Unsteady shear flows of colloidal hard-sphere suspensions by dynamic simulation

Stéphanie Marenne and Jeffrey F. MorrisDavid R. Foss and John F. Brady

Citation: Journal of Rheology **61**, 477 (2017); doi: 10.1122/1.4979005
View online: http://dx.doi.org/10.1122/1.4979005
View Table of Contents: http://sor.scitation.org/toc/jor/61/3
Published by the The Society of Rheology

Unsteady shear flows of colloidal hard-sphere suspensions by dynamic simulation

Stéphanie Marenne and Jeffrey F. Morris[a)]

Benjamin Levich Institute and Department of Chemical Engineering, CUNY City College of New York, New York, New York 10031

David R. Foss and John F. Brady

Division of Chemistry and Chemical Engineering, California Institute of Technology, Pasadena, California 91125

(Received 11 August 2016; final revision received 22 January 2017; published 5 April 2017)

Abstract

The rheology during the start-up and cessation of simple shear flow has been investigated for near hard-sphere colloidal suspensions. Simulations augmented by theoretical analysis are used to determine how the non-Newtonian stress development and relaxation depend on the microstructure. Accelerated Stokesian dynamics (ASD) and Brownian dynamics (BD) simulations are used for $0.05 \leq Pe \leq 500$ in concentrated freely flowing suspensions; the Péclet number defining the ratio of shear to thermal motion is $Pe = 3\pi\eta\dot{\gamma}a^3/kT$ with η the suspending fluid viscosity, $\dot{\gamma}$ the shear rate, and kT the thermal energy. Theoretical predictions based on the Smoluchowski equation for dilute suspensions are made, and these are primarily used for comparison with results from BD simulations in which hydrodynamic interactions are neglected. For suspensions with hydrodynamics, simulations by ASD are used to probe start-up and flow cessation over a large range of Pe; these studies focus on solid volume fraction $\phi = 0.4$, with more limited examinations at other ϕ. The use of both BD and ASD simulations allows us to discriminate hydrodynamic interaction effects on the suspension rheology. The Brownian stresses computed by either method exhibit overshoots of their steady state value during the start-up of shear flow. The overshoots occur at strain amplitudes which depend on Pe, and the overshoot is described by a model based on extension of the concept of cage-breaking from glass dynamics. Results from the relaxation of a sheared suspension show that the distortion of the pair distribution function from its equilibrium form has a fast radial relaxation and a slow angular relaxation. The various rheometric functions (relative viscosity; first and second normal stress differences) are found to respond on different timescales, reflecting their different dependences on the flow-induced structure. A re-examination of steady shear flow allows us to find normal stress differences which tend properly toward zero at small Pe, unlike prior work; the discrepancy is found to be due to finite size scaling, as small simulations used in prior work resulted in excessively large normal stress responses at small Pe. © *2017 The Society of Rheology*. [http://dx.doi.org/10.1122/1.4979005]

I. INTRODUCTION

Suspensions of colloidal particles occur in a number of materials including paints, cements, and coatings. In these applications, the rheological properties are naturally of central concern. Our interest in this work is in how the properties of colloidal dispersions develop in start-up of flow and how they relax upon flow cessation. These transient flow processes provide insight to the interplay of the various forces within the material, here examined for the hard-sphere Brownian dispersion in Newtonian liquid. Studying this ideal case allows us to use well-developed simulation tools to probe the micromechanical scale, in order to relate the transient stresses to the evolving particle arrangement. The work is intended to provide a baseline on the most basic system, with insights gained from this system providing guidance to phenomena seen in progressively more complex fluids.

For monodisperse hard sphere dispersions, the two defining parameters are the particle volume fraction, ϕ, and the Péclet number $Pe = 3\pi\eta a^3\dot{\gamma}/kT$, which represents the relative strength of shear flow to Brownian motion; here η is the suspending fluid viscosity, a is the particle radius, $\dot{\gamma}$ is the shear rate, and kT is the thermal energy. The influence of flow under dilute conditions has been the most developed. The arrangement of the particles, or microstructure, is driven from its isotropic equilibrium form at $Pe = 0$ to a highly anisotropic structure at large Pe, showing the importance of the balance of the various mechanisms driving particle motion.

The approach to analysis of the microstructure of flowing Brownian suspensions was pioneered by Batchelor [1]. This approach considers directly the probability distribution function governing the configurations in the suspension, and this essentially statistical mechanical approach develops the Smoluchowski partial differential equation (PDE) analysis of the pair correlation function, which is statistically equivalent to the Langevin stochastic PDE [2,3], upon which discrete-particle simulations tools used in this work are based. The Smoluchowski approach has proven useful for description of the steady shear flow of hard-sphere suspensions in the dilute limit at low Pe [4–7] and at high Pe [8]. Simulations by Stokesian dynamics have been performed to investigate the steady shear properties of freely flowing hard-sphere colloidal suspensions at low and intermediate Pe [9,10], as well as

a)Author to whom correspondence should be addressed; electronic mail: morris@ccny.cuny.edu

© 2017 by The Society of Rheology, Inc.

at high Pe and high ϕ [11,12]. Simulation has provided understanding to allow rational extension of Smoluchowksi theory to elevated ϕ for the entire range of Pe [13].

However, there is a very notable lack of information on the behavior of colloidal hard-sphere dispersions in time-dependent shear flows. Time-dependent shear flows encompass a range of topics, many well-established in their analysis such as creep and recovery, or linear viscoelastic response (LVR or small angle oscillatory shear, SAOS), while others are more recent and remain under development including large amplitude oscillatory shear (LAOS) [14]. Here, we focus on start-up and cessation of shear flow for varying strengths of the shear to Brownian motion, or Pe, in concentrated suspensions. Our work applies Brownian dynamics, in which hydrodynamic interactions (HI) are neglected, as well as the accelerated Stokesian dynamics (ASD) algorithm [15], in which full hydrodynamics are incorporated, to simulate the suspension flow. The Brownian dynamics results are more directly comparable to the simplified Smoluchowski theory, in which we neglect HI. Our use of Stokesian dynamics allows us to validate the large-strain behavior of the system against well-established results, which themselves compare favorably against steady shear experiments of near-hard sphere dispersions, e.g., D'Haene *et al*. [16], as well as van der Werff *et al*. [17].

The start-up of shear flow has been examined experimentally in colloidal dispersions of hard spheres by D'Haene *et al*. [16], on coating suspensions and fumed silica by Yziquel *et al*. [18] and in glassy systems of hard spheres by Koumakis *et al*. [19], Laurati *et al*. [20], Amann *et al*. [21], and Koumakis *et al*. [22]. Each of these studies finds the stress to overshoot its eventual steady state value. For these glassy systems, this was shown to be reproducible by simulations and the overshoots can also be predicted by mode-coupling theory [21,23]. Although we observe a similar behavior qualitatively for freely flowing suspensions, the large difference in particle concentration changes the dynamics of the fluid and makes a direct comparison difficult [24,25]. Whereas the start-up of shear flow provides insight into the buildup of the particle microstructure, structural decay is probed following the abrupt cessation of flow. This structure relaxation has been studied by Mackay and coworkers [26,27] in stress jump experiments which allow identification of the separate viscous (hydrodynamic) and elastic (thermodynamic) parts of the stress. For glassy systems, the relaxation of the residual stress after cessation of shear flow has been studied by Ballauff *et al*. [28], but in this work, due to the high concentration of particles, the relaxation shows a different behavior.

Recent advances in computational power open two avenues. First, in revisiting the earlier work to compare against existing results for steady shear flow, we find that using a larger system size (i.e., more particles in the replicated computational unit cell), we are able to better resolve the behavior of small-Pe concentrated suspensions. Here, prior work had difficulty in obtaining the expected tendency of normal stress differences toward zero as $Pe \to 0$. This issue is found to be a result of the smaller (by more than an order of magnitude in number, or a factor of between two and three in linear dimension) computational cells in earlier work [9,10], as discussed in Sec. V A. Second, and directly related to the primary objective of this work, the availability of many equivalent processors in computational clusters allows us to conveniently examine the transient behavior by the ensemble approach: We use many identically prepared replicas of the system to which the same flow conditions are applied, and from the average and fluctuations over the many replicas, typically $O(1000)$, we extract the properties of the dispersion. This differs from the approach used in simulational determination of the steady properties, where the reasonable assumption of ergodicity allows averaging over a simulation for extended time—such an approach clearly is not appropriate to determine the time dependent behavior.

As this is a rather extended work employing several methods, we provide a detailed outline and a description of primary findings in Sec. I A.

A. Outline and key findings

Following this section in which we outline findings of this work, there follows immediately Sec. II which develops the microstructural analysis based on the Smoluchowski equation; this serves as the conceptual basis for describing flow distortion of the particle microstructure. The resulting stress and a generalization of existing theory [8] to unsteady flows are described in Sec. III, with mathematical details of the solutions deferred to Appendices. This work is centered on novel results from simulation, and in Sec. IV, we briefly describe the ASD and Brownian dynamics (BD) simulation approaches used; because we apply a true ensemble averaging, some attention to the system size and necessary number of replicas of a given condition for statistical reliability of various results is given here. Note that ASD incorporates HI, which are neglected in the BD simulations. In Sec. V, we provide the results of our study with comparison of theory and simulation where possible. Comparison is most readily made between dilute Smoluchowski analysis (developed in Sec. III and the Appendixes) and the BD results, as hydrodynamic effects may be eliminated in the theory. By comparison of results from BD and ASD, we are then able to distinguish effects that are clearly due to HI and those which follow from the balance of shear flow and Brownian motion.

Our results fall in three categories: (1) Examination of steady shear properties, (2) near-equilibrium studies based on application of Green-Kubo theory to the simulation results and comparison with weak perturbation theory of the Smoluchowski equation, and (3) transient dynamics in start-up of shear flow and following cessation of the shear flow. The steady shear results revisit prior work [10] in order to demonstrate that the small particle numbers in earlier computations strongly affected small-Pe properties of the suspension, thus providing some indication of the necessary scale of the computational cell for reliable results, at least within the range of solid fraction studied here. The near-equilibrium studies allow examination of the role of HI through study of the high-frequency dynamic modulus, conveniently examined through the short-time response of the shear stress autocorrelation function. The start-up and cessation of shear flow

of suspensions has seen limited prior study and we have thus focused on these topics, which provide insight to the particle organization process at the microstructural scale and its relation to the stress response. The transient results are first presented through an example illustrating our standard protocol, in which we simulate an ensemble starting from the equilibrium (quiescent) state to steady state at the specified Pe, and then stop flow and monitor the relaxation of the structure and stress. This is followed by comparison of results highlighting the difference between ASD and BD (with and without HI, respectively) for the start-up flow and for cessation of shear flow, and then a more complete development of the results from ASD simulations. This last section describes both the viscometric functions and microstructure, considering in detail how the evolution with time of the neighbor cage, a concept well-known in study of glassy dynamics [19–23] and central to mode-coupling theory of dense colloidal suspensions [29,30], plays a role in freely flowing suspensions. We will briefly note several key findings of this work here, with details in Sec. V.

One key finding of this study that does not involve transient flow is the noted system size dependence of results. A second is the role of HI on near-equilibrium results; these show that the Smoluchowski theory accurately predicts the shear stress of the BD system in the near-equilibrium case and the expected scalings are found at short times after the start-up and after cessation of shear flow. However, we are able to show that the effect of HI is to induce not simply a quantitative change, but different scalings for the short time behavior of suspensions, particularly through the high-frequency dynamic modulus, G'_∞. Our work shows that the near-equilibrium behavior is connected to the transient dynamics at arbitrary Pe through the growth of the elastic Brownian stress being given by the product of G'_∞ and the imposed strain for small strain after start-up: Deviation from this behavior then provides insight to the onset of nonlinear response of the suspension. The work as a whole provides thorough insight to the role of HI in the development of the suspension properties, as just noted for the near-equilibrium suspension. This aspect is more obvious for high Pe, where neglect of HI results in an inability to capture shear thickening in BD. One aspect of the transient dynamics which is independent of HI is striking. Specifically, the relaxation of the Brownian shear stress after flow cessation has a rapid portion which depends on the level of structural distortion (and hence on Pe) in the near-contact boundary layer, but following this rapid relaxation, the relaxation curves of the stress response for all Pe collapse to a single curve.

The overall picture developed in this work is that the excluded volume interactions between particles, when taken together with a shear flow, play a pronounced role in development of a structure with multiple length scales, and this induces dynamics which have a range of inherent timescales. A key finding regarding the relaxation dynamics for the suspensions with full hydrodynamics is that the first normal stress difference N_1 has a significantly longer relaxation time scale (as does the shear stress) than the second normal stress difference N_2, indicating that it is dependent on longer range microstructural features than N_2. This highlights the importance of considering both small-scale features of the microstructure such as the $O(Pe^{-1}a)$ thickness boundary layer [8] in which diffusive dynamics result in a rapid relaxation and the long-range probability wake, where diffusion on the particle scale a requires a much longer time. All of the viscometric functions, i.e., the apparent viscosity, N_1 and N_2 exhibit overshoots in the start-up flow at strains of $O(1)$ for $\phi = 0.4$ and we show that this overshoot can be traced to the particle cage concept, which we have statistically defined based on the nearest neighbor ring in the pair distribution function. The cage distortion and breakage are illustrated and related to the stress response.

II. MICROSTRUCTURE

We consider the stress and its relation to the microstructure of a sheared suspension. We begin with an analytical approach to the microstructure, based on the Smoluchowski equation, to provide a framework for understanding the competing effects governing the suspension flow. Recall that the Smoluchowski theory and Langevin descriptions are statistically equivalent at timescales larger than the particle inertial timescale [2].

For a suspension of N identical spheres in a Newtonian fluid subjected to Stokes shear flow $\mathbf{U}^\infty = \dot{\mathbf{\Gamma}} \cdot \mathbf{x}$ with velocity gradient tensor $\dot{\mathbf{\Gamma}}(t)$, the configurational probability $P_N(\mathbf{x}^N, t)$ satisfies the Smoluchowski equation

$$\frac{\partial P_N}{\partial t} + \sum_{\alpha=1}^{N} \nabla_\alpha \cdot \mathbf{j}_\alpha = 0, \tag{1}$$

with the flux of probability associated with particle α given by

$$\mathbf{j}_\alpha = \mathbf{U}_\alpha P_N - \sum_{\beta=1}^{N} \mathbf{D}_{\alpha\beta} P_N \cdot \nabla_\beta (\ln P_N + V). \tag{2}$$

Here, $\mathbf{U}_\alpha$ is the velocity of particle α, V is the interparticle potential energy made dimensionless with the thermal energy kT, and the Brownian diffusivity for the relative motion of two particles is given by $\mathbf{D}_{\alpha\beta} = kT\mathbf{M}_{\alpha\beta}$, where $\mathbf{M}_{\alpha\beta}$ is the hydrodynamic mobility of particle α due to a force exerted on particle β. The translational velocity of particle α is given by

$$\mathbf{U}_\alpha = \dot{\mathbf{\Gamma}} \cdot \mathbf{x}_\alpha + (\mathbf{R}_{\mathbf{FU}}^{-1} \cdot \mathbf{R}_{\mathbf{FE}} : \langle \mathbf{E} \rangle)_\alpha,$$

where $\mathbf{R}_{\mathbf{FU}}$ and $\mathbf{R}_{\mathbf{FE}}$ are the many-body hydrodynamic resistance tensors that give the hydrodynamic force on a particle due to its motion relative to the fluid and due to an imposed rate of strain, respectively, and $\mathbf{E} = (\dot{\mathbf{\Gamma}} + \dot{\mathbf{\Gamma}}^{\mathrm{T}})/2$ is the rate-of-strain portion of the bulk velocity gradient (the superscript T denotes the transpose). Although angular displacements are present due to flow and Brownian motion and are relevant in the dynamics which generate the microstructure, for spheres the angular variables are not relevant to the description of the microstructure and thus only spatial derivatives are present in Eqs. (1) and (2).

Equation (1) is formally reduced to pair-particle level by integrating with respect to the center-of-mass coordinate of a pair of particles and the positions of the remaining $N-2$ particles. This yields the equation for $P_{1|1}(\mathbf{r})$, the probability distribution for finding a particle at $\mathbf{r}$ given that a particle lies at the origin

$$\frac{\partial P_{1|1}}{\partial t}+\nabla_r\cdot\left(\langle\mathbf{U}\rangle_2 P_{1|1}\right)-\nabla_r\cdot\left[P_{1|1}\langle\ln P_N+V)\rangle_2\right]-\nabla_r\cdot P_{1|1}\times\int P_{3|2}(\mathbf{x}_3|\mathbf{r})\langle(\mathbf{D}_{13}-\mathbf{D}_{23})\cdot\nabla_3(\ln P_N+V)\rangle_3 d\mathbf{x}_3=0, \tag{3}$$

where $\nabla_r=\nabla_2=-\nabla_1$, and $P_{3|2}$ is the probability of finding a third particle at $\mathbf{x}_3$ given the positions of two particles. In Eq. (3), $\langle\rangle_2$ indicates a conditional average with two particles fixed and the relative velocity and relative diffusivity are given by

$$\mathbf{U}=\mathbf{U}_2-\mathbf{U}_1 \quad \text{and} \quad \mathbf{D}=\mathbf{D}_{11}-\mathbf{D}_{12}-\mathbf{D}_{21}-\mathbf{D}_{21}-\mathbf{D}_{22},$$

respectively. It is convenient to work with the pair distribution function $g(\mathbf{r})=P_{1|1}(\mathbf{r})/n$, with n the uniform particle number density.

Quantities are made dimensionless by the scalings

$$\mathbf{r}\sim a, \quad \mathbf{U}\sim\dot{\gamma}a, \quad \mathbf{D}\sim 2D, \quad \text{and} \quad t\sim a^2/2D,$$

where $\dot{\gamma}=|\dot{\mathbf{\Gamma}}|$ is the magnitude of the velocity gradient tensor, and the relative diffusivity is scaled with the far-field asymptotic value for isolated particles $2D$, with $D=kT/6\pi\eta a$ the diffusivity of an isolated particle of radius a and thermal energy kT in a fluid of viscosity η. The relative importance of shear and Brownian motion is given by the Péclet number

$$Pe=\frac{\dot{\gamma}a^2}{2D}=\frac{3\pi\eta a^3\dot{\gamma}}{kT}.$$

Qualitative features of the microstructural development can be obtained from a dilute two-particle analysis. The dimensionless equation and associated boundary conditions governing $g(\mathbf{r})$ are

$$\frac{\partial g}{\partial t}+Pe\nabla\cdot(\mathbf{U}g)-\nabla\cdot(\mathbf{D}\nabla g)=0, \tag{4a}$$

$$\hat{\mathbf{r}}\cdot\mathbf{D}\cdot\nabla g(\mathbf{r})=Pe\,\hat{\mathbf{r}}\cdot\mathbf{U}g(\mathbf{r}) \quad \text{at } r=2, \tag{4b}$$

$$g\sim 1 \quad \text{as } r\to\infty, \tag{4c}$$

where $\hat{\mathbf{r}}=\mathbf{r}/r$ is the unit vector along the line of centers from particle 1 to particle 2. To simplify here and below, we write ∇ for ∇_r. The angle brackets indicating averaging are not needed in the dilute limit.

At equilibrium, or $Pe=0$, $g(\mathbf{r})$ is isotropic. In the case of pure hydrodynamics (hard spheres at $Pe^{-1}=0$), the pair-distribution function for shearing motion has fore-aft symmetry in the shear plane [31], a result of Stokes-flow reversibility. At finite Pe, the differing balances of Brownian motion and shear flow at different positions introduce irreversibility and the fore-aft symmetry of $g(\mathbf{r})$ is broken. There is accumulation of particles close to contact near the compressional axis and a depletion zone in the extensional quadrant, giving rise to non-Newtonian normal stresses. Any symmetry breaking agent is found to give rise to finite normal stress differences as $Pe\to\infty$, implying the pure hydrodynamic limit is singular [8].

III. STRESS FORMULATION AND ANALYSIS

A. Bulk stress

The bulk stress of the colloidal suspension is

$$\langle\mathbf{\Sigma}\rangle=-\langle p\rangle_f\mathbf{I}+2\eta\mathbf{E}^\infty-nkT\mathbf{I}+n\{\langle\mathbf{S}^E\rangle+\langle\mathbf{S}^B\rangle+\langle\mathbf{S}^P\rangle\}, \tag{5}$$

where $-\langle p\rangle_f\mathbf{I}$ is the isotropic pressure term from the fluid phase. The number density of particles n can be related to simulation variables as $n=N/V$ with N being the number of particles in the simulation and V the volume of the simulated periodic box. The first two terms represent the fluid contribution to the stress and the remainder is due to the particles, also including a pressure contribution [32,33].

Defining the stresslet generally as the single-body contribution to the bulk stress, the hydrodynamic stresslet is given by $\langle\mathbf{S}^E\rangle=-\langle\mathbf{R}_{SU}\cdot(\mathbf{U}-\mathbf{U}^\infty)-\mathbf{R}_{SE}:\mathbf{E}^\infty\rangle$, where $\mathbf{R}_{SU}$ and $\mathbf{R}_{SE}$ yield the coupling of stress to velocity and rate of strain, respectively. The interparticle force stresslet is $\langle\mathbf{S}^P\rangle=\langle-\mathbf{R}_{SU}\cdot\mathbf{R}_{FU}^{-1}\cdot\mathbf{F}^P-\mathbf{x}\mathbf{F}^P\rangle$. The Brownian stresslet, which captures the influence of the particle configuration relaxing toward its equilibrium form, is $\langle\mathbf{S}^B\rangle=-kT\langle\nabla\cdot(\mathbf{R}_{SU}\cdot\mathbf{R}_{SU}^{-1})\rangle$. The total particle contribution to the bulk stress is

$$\langle\mathbf{\Sigma}^{\mathrm{p}}\rangle=-nkT\mathbf{I}+n\{\langle\mathbf{S}^E\rangle+\langle\mathbf{S}^B\rangle+\langle\mathbf{S}^P\rangle\}, \tag{6}$$

and may be rewritten as [32]

$$\langle\mathbf{\Sigma}^{\mathrm{p}}\rangle=-nkT\mathbf{I}+n^2kTa\oint_{|\mathbf{r}|=2a}\hat{\mathbf{r}}\hat{\mathbf{r}}g(\mathbf{r})d\mathbf{S}-n\langle\mathbf{x}\mathbf{F}_p\rangle-n\langle\mathbf{R}_{SU}\cdot\mathbf{R}_{FU}^{-1}\cdot\mathbf{R}_{FE}-\mathbf{R}_{SE}\rangle:\langle\mathbf{E}^\infty\rangle+nkT\langle\mathbf{R}_{SU}\cdot\mathbf{R}_{FU}^{-1}\cdot\nabla[V+\ln P_N]\rangle \tag{7}$$

by decomposing $\langle\mathbf{S}^B\rangle$ into the contact integral and the final term involving $\nabla\ln P_N$.

Distortion of the microstructure from isotropy caused by shearing leads to normal stress differences, defined as

$$N_1=\Sigma^p_{xx}-\Sigma^p_{yy} \quad \text{and} \quad N_2=\Sigma^p_{yy}-\Sigma^p_{zz}. \tag{8}$$

The individual stress components Σ^p_{xx}, Σ^p_{yy}, and Σ^p_{zz} are generally accepted to be negative for colloidal hard-sphere suspensions [34], i.e., these are compressive. Brady and Vicic [6] found by an analytical approach that $N_1>0$ and $N_2<0$ at low Pe. Brady and Morris [8] analyzed colloidal suspensions under strong shear flow and found $N_1<0$ and $N_2<0$ at high Pe. Stokesian dynamics simulations of Foss and Brady [10] agreed with those predictions at low and high Pe. This

behavior for N_2 is consistent with experiment, yet there remains some experimental uncertainty regarding the sign of N_1 in the limit $Pe^{-1}=0$, as Zarraga *et al.* [35] and Dai *et al.* [36] found $N_1<0$, while Dbouk *et al.* [37] found $N_1>0$. The latter is a "dilatant" response in the sense that the plates of a torsional device are pushed apart by the flow-induced normal stress. This behavior is expected for abruptly shear-thickening suspensions, but even in this case the evidence is contradictory: $N_1>0$ is found experimentally by Lootens *et al.* [38] and in simulations by Mari *et al.* [39], while experiments by Cwalina and Wagner [40] found $N_1<0$. Royer *et al.* [41] recently observed a transition from $N_1<0$ to $N_1>0$ with increase of the shear rate at large ϕ, and have argued this is indicative of a transition from dominance of lubricated to frictional interactions between particles.

B. Green-Kubo theory

We consider the relaxation of fluctuations from equilibrium through the decay of the shear-stress autocorrelation function in a quiescent suspension, focusing on how HI affect the short time behavior. The steady solution to Eq. (4) in the absence of flow is $g=1$ everywhere, and thus the mean particle stress is isotropic, the osmotic pressure. However, Brownian motion produces fluctuations that cause temporary deviations in the microstructure from isotropy, and thus the shear stress in the system at any time deviates from its time average of zero. Consider the shear-stress autocorrelation function

$$C_s(t)=\langle\sigma_{xy}(t)\sigma_{xy}(0)\rangle, \tag{9}$$

where σ_{xy} represents a shear stress due to a fluctuation. We use the subscript xy for clarity, but since there is no preferred direction at equilibrium, we could also use xz or yz. Note that in terms of stresses in Eq. (6), σ_{xy} could represent either the interparticle force or Brownian contribution; as defined, the hydrodynamic contribution is strictly proportional to an imposed rate of strain and is identically zero under quiescent conditions.

The relationship between the autocorrelation function in Eq. (9) and the suspension rheology given by Green-Kubo formulae is well established [42,43]. Specifically, the frequency-dependent complex viscosity due to an oscillatory shear flow is related to $C_s(t)$ by [44]

$$\eta(\omega)=\eta'(\omega)-i\eta''(\omega)=\eta'_\infty+\frac{V}{kT}\int_0^\infty C_s(t)e^{-i\omega t}dt, \tag{10}$$

where the real part corresponds to dissipation and the imaginary part to elasticity. Here, V is the volume of the suspension and $\eta'_\infty(\phi)$ is the high-frequency dynamic viscosity given by the hydrodynamic contribution, $\mathbf{S}^E$, in an equilibrium microstructure. The complex modulus can also be calculated from Eq. (10) by

$$G'(\omega)=\omega\eta''(\omega)\quad\text{and}\quad G''(\omega)=\omega\eta'(\omega). \tag{11}$$

Thus, the high-frequency elastic shear modulus, $G'_\infty=G'(\omega\to\infty)$ is given by

$$G'_\infty=\frac{V}{kT}C_s(0).$$

Other properties of $C_s(t)$ can be found by analyzing the microstructure in the presence of small amplitude oscillatory shear flow characterized by the time-dependent rate of strain tensor

$$\langle\mathbf{E}\rangle=\dot\gamma\hat{\mathbf{E}}e^{i\alpha t},$$

where $\alpha=\omega a^2/2D$ is the frequency made dimensionless by $a^2/2D$ and $\hat{\mathbf{E}}$ is the rate of strain made dimensionless with $\dot\gamma$. The resultant perturbation to the equilibrium structure, $f=g-1$, is linear in $\hat{\mathbf{E}}$, i.e.,

$$f(\mathbf{r},t)=-\frac{1}{2}Pef(r)e^{i\alpha t}\hat{\mathbf{r}}\cdot\hat{\mathbf{E}}\cdot\hat{\mathbf{r}}, \tag{12}$$

because $Pe\ll 1$ due to the small amplitude of the shear. Substitution of Eq. (12) into the pair-evolution equation (4) gives, to leading order in Pe,

$$-i\alpha f+\nabla\cdot\mathbf{D}\cdot\nabla f=\nabla\cdot\mathbf{U}, \tag{13a}$$

$$\hat{\mathbf{r}}\cdot\mathbf{D}\cdot\nabla f=\hat{\mathbf{r}}\cdot\mathbf{U}\ \text{at}\ r=2, \tag{13b}$$

$$f\sim 0\ \text{as}\ r\to\infty, \tag{13c}$$

whose solution has been discussed at length elsewhere [32,45]. Here, we are interested in the short-time behavior of $C_s(t)$, which corresponds to the high-frequency behavior of f.

As $\alpha\to\infty$, the solution is $f=0$: The arbitrarily high-frequency and small-amplitude forcing does not disturb the equilibrium structure. The perturbation around infinite frequency is, however, singular, with a boundary layer in which unsteadiness balances diffusion in order to satisfy the no-flux boundary condition at contact. In the absence of HI, the dimensionless relative diffusivity between two particles is simply the constant $\mathbf{I}$, and there is a balance $\alpha f\sim\partial^2 f/\partial r^2$, resulting in a boundary layer at contact that scales as $(r-2a)/a\sim\alpha^{-1/2}$. The result of this thin boundary layer near the surface is a contact value of the perturbation function f, and thus a complex viscosity, that decays as $\alpha^{-1/2}$ for $\alpha\gg 1$. From Eq. (11) this results in an elastic modulus, G', that grows as $\alpha^{1/2}$ as $\alpha\to\infty$, as has been widely reported in the literature [32,46]. Thus, from Eq. (10) it can be determined that $C_s(t)$ diverges at short times [45] proportional to $t^{-1/2}$.

HI qualitatively change this behavior. With inclusion of HI the boundary layer at contact in which frequency balances diffusion has thickness that scales as α^{-1}, rather than $\alpha^{-1/2}$, because the relative diffusivity vanishes at contact as $(r-2a)/a$. This scaling of the boundary layer results in a qualitatively different rheological response. In this case, the contact value of f and the complex viscosity both decay at high frequencies as α^{-1}. The stronger decay of the complex viscosity means that the elastic modulus, G', now approaches a

constant as $\omega \to \infty$. $C_s(t)$ approaches a constant as $t \to 0$ and its initial decay is linear with time as in the case with a soft, but steep, interaction potential [47]. As a final note, the long time (or low frequency) decay of the viscosity is predicted to behave as $t^{-7/2}$ with or without HI (the coefficient changes with hydrodynamics [45]). This $t^{-7/2}$ behavior is the diffusive decay of the quadrupolar disturbance (12) caused by weak shear flow.

C. Nonequilibrium behavior

We can calculate the steady state solution to Eq. (4) for the case of suspensions undergoing strong shear without HI. This section presents only the principal results of the analytical development; the solution procedure can be found in Appendix A. The steady-state solution to the radial-balance approximation [8] as described there is

$$g_{ss}(y) = \frac{1 + 2\gamma_r \int_0^y e^{s(z)} dz}{1 + 2\gamma_r \int_0^\infty e^{s(z)} dz},$$

where $s(z)$ is given by

$$s(z) = 2\gamma_r \left[\left(1 - \frac{1}{2\gamma_r} Pe^{-1} \right) z + \frac{1}{4} Pe^{-1} z^2 \right],$$

with $\gamma_r = \hat{\mathbf{r}} \cdot \hat{\mathbf{E}} \cdot \hat{\mathbf{r}}$. Here, $g_{ss}(y)$ is valid only for $\gamma_r < 0$, i.e., in the compressional quadrants; in the extensional quadrants, where $\gamma_r > 0$, g remains $O(1)$ and there is no boundary layer. Rewriting g as

$$g_{ss}(y) = g_{ss}(0) \left[1 + \gamma_r \int_0^y e^{s(z)} dz \right],$$

with

$$g_{ss}(0) = -\frac{4}{3} Pe \gamma_r + O(1) \quad \text{as } Pe \to \infty, \tag{14}$$

shows that there is an $O(1)$ excess of particles in the boundary layer at contact, as seen by taking the product of $g_{ss} \sim O(Pe)$ with the $O(Pe^{-1}a^3)$ boundary layer volume.

Using this result for the pair-distribution function, the stress in the absence of HI for a hard-sphere potential is given by the contact integral in Eq. (7)

$$\langle \boldsymbol{\Sigma}^p \rangle = -nkT\mathbf{I} + \eta\dot{\gamma}\phi^2 \frac{9}{\pi} \int_{\gamma_r<0} \hat{\mathbf{r}}\hat{\mathbf{r}} \gamma_r d\Omega + O(Pe^{-1}). \tag{15}$$

While the hard-sphere force is of magnitude kT, the large $O(Pe)$ pair probability in the compressive quadrants results in a viscous $O(\eta\dot{\gamma})$ stress independent of kT as $Pe \to \infty$.

Although we have neglected $O(Pe^{-1})$ terms on the right-hand side of Eq. (A3a) in the radial-balance approximation described in Appendix A, these terms have only a slight quantitative effect on the results [6]; the important qualitative (and even quantitative) effects are captured by the radial balance, which will now be applied in an examination of the unsteady boundary-layer problem.

1. Start-up of flow

Equation (4) has also been solved for start-up of shear flow. The complete solution can be found in Appendix B. To calculate the stresses, we only need the value of $g(\mathbf{r})$ at contact. At short times, it has the asymptotic form

$$g(0,t) \sim 1 - \frac{16}{\pi^{1/2}} \gamma_r^3 Pe^3 t^{1/2} \quad \text{as } t \to 0, \tag{16}$$

where $\gamma_r < 0$, showing that the initial growth of the boundary-layer microstructure scales as $t^{1/2}$, similar to the behavior near equilibrium (cf. Sec. III B). The large exponent on Pe in Eq. (16) indicates that this limit is only strictly valid at very short times, of $O(Pe^{-4})$ or smaller. We have not been able to determine whether the $t^{1/2}$ behavior persists to longer (more rheologically significant) times.

At long times, the system reaches the steady state solution (14) exponentially as

$$g(0,t) \sim 1 - \frac{4}{3} \gamma_r Pe (1 - e^{3\gamma_r Pe t}) \quad \text{as } t \to \infty, \tag{17}$$

and again we recall this is valid where the pair radial velocity is negative, i.e., where $\gamma_r < 0$. It is evident from Eq. (17) that the appropriate time scale at long times is $(a^2/2D)Pe^{-1}$, or simply the flow time $\dot{\gamma}^{-1}$.

2. Flow cessation

Flow cessation is a simpler mathematical problem than start-up as the microstructure decays through Brownian diffusion in the absence of an imposed flow, i.e., γ_r is zero once the flow stops. This parameter does, however, enter as a parameter in the initial condition for the decay of the structure. For the dilute limit, which is considered in this analysis, the only relevant time scale is the time for a particle to diffuse the width of the boundary layer. At higher concentrations, the relaxation also involves the closure of the wake in the extensional quadrant, for which particles must diffuse a distance on the order of their own size. The response at contact of $f = g - 1$ for the dilute case is calculated in Appendix C and is given by

$$f(0,\tau) = -g_{ss}(0) e^{4\gamma_r^2 \tau} \operatorname{erfc}\left(\sqrt{4\gamma_r^2 \tau} \right). \tag{18}$$

IV. SIMULATION METHODS

Two simulation methods are used. These are BD [48], in which HI are neglected with fluid mechanical effects included only through the single-particle Stokes drag, and ASD including Brownian motion [15], where full HI are included. A brief overview of each method follows.

A. ASD simulations

The ASD simulations are based on the N-body Langevin equation

$$\mathbf{m}\cdot\frac{d\mathbf{U}}{dt}=\mathbf{F}^{E}+\mathbf{F}^{B}+\mathbf{F}^{P}, \tag{19}$$

where $\mathbf{m}$ is the $6N\times 6N$ generalized mass-moment of inertia matrix and $\mathbf{U}$, a $6N$-vector, is the combined translational and rotational velocity of the particles. The "forces" on the right-hand side include also torques and are thus $6N$-vectors. The hydrodynamic forces $\mathbf{F}^{E}$ arise from interactions between particles. The Reynolds number is assumed to be vanishingly small at the particle scale, so that linear relations between the forces and the motions hold, e.g., $\mathbf{F}^{E}=-\mathbf{R}_{FU}\cdot(\mathbf{U}-\mathbf{U}^{\infty})+\mathbf{R}_{FE}:\mathbf{E}^{\infty}$. For each particle α, $\mathbf{U}_{\alpha}^{\infty}=\dot{\mathbf{\Gamma}}\cdot\mathbf{x}_{\alpha}$ is calculated according to its position $\mathbf{x}_{\alpha}$. The resistance matrices $\mathbf{R}_{FE}$ and $\mathbf{R}_{FU}$ depend only on the configuration of the particles. $\mathbf{F}^{B}$, the Brownian forces, are computed in accord with the fluctuation-dissipation theorem: $\overline{\mathbf{F}^{B}(0)}=0$ and $\overline{\mathbf{F}^{B}(0)\mathbf{F}^{B}(t)}=2kT\mathbf{R}_{FU}\delta(t)$. $\mathbf{F}^{P}$, the interparticle forces, are typically conservative (derivable from a potential) but can be frictional or hard-sphere forces.

Equation (19) is valid provided that the change in configuration of the particles $\mathbf{x}$ is small during the timescale of the Brownian motion: $\tau=m/(6\pi\eta a)$ with m the mass of a particle. Integrating Eq. (19) twice in time, we obtain [49]

$$\begin{aligned}\Delta\mathbf{x}=Pe\{\mathbf{U}^{\infty}+\mathbf{R}_{FU}^{-1}\cdot\left[\mathbf{R}_{FE}:\mathbf{E}^{\infty}+\dot{\gamma}^{*-1}\mathbf{F}^{P}\right]\}\Delta t\\+\nabla\cdot\mathbf{R}_{FU}^{-1}\Delta t+\mathbf{X}(\Delta t),\end{aligned} \tag{20}$$

with $\bar{\mathbf{X}}=0$ and $\overline{\mathbf{X}(\Delta t)\mathbf{X}(\Delta t)}=2\mathbf{R}_{FU}^{-1}\Delta t$. In Eq. (20), $\Delta\mathbf{x}$ is the change in particle position during Δt and $\mathbf{X}(\Delta t)$ is a random displacement due to Brownian motion. The nondimensional shear rate $\dot{\gamma}^{*}=6\pi\eta a^{2}\dot{\gamma}/|\mathbf{F}^{P}|$ measures the relative strength of the shearing and interparticle forces. Because we model hard-sphere suspensions here, there are no interparticle forces $\mathbf{F}^{P}$ (i.e., $\dot{\gamma}^{*-1}=0$). Thus, the relevant forces are the hydrodynamic and the thermal forces.

B. BD

BD again begins from the Langevin equation. The algorithm used here is based on the method of Heyes and Melrose [50,51] for simulation of hard spheres in the absence of HI. Motions are governed by the particle evolution equation

$$\begin{aligned}&\Delta\mathbf{x}=\mathbf{U}^{\infty}\Delta t+\Delta\mathbf{x}^{HS}+\mathbf{X}(\Delta t),\\&\bar{\mathbf{X}}=0,\quad\text{and}\quad\overline{\mathbf{X}(\Delta t)\mathbf{X}(\Delta t)}=2D_{0}\mathbf{I}\Delta t.\end{aligned} \tag{21}$$

Here, $\Delta\mathbf{x}$ is the change in particle position during the time step Δt, $\mathbf{U}^{\infty}\Delta t=\dot{\mathbf{\Gamma}}\cdot\mathbf{x}\Delta t=y\hat{\mathbf{x}}\Delta t$ for simple-shear flow and $\mathbf{X}(\Delta t)$ is a Brownian motion-induced displacement with zero mean and covariance related to the Stokes–Einstein diffusivity for a single particle alone in the fluid. After the Brownian and affine displacements are applied, particle overlaps are determined. Any overlapping particles are displaced along their line of centers according to

$$\Delta\mathbf{x}^{HS}=\frac{1}{2}(\Delta r-2)\hat{\mathbf{r}}H(2-\Delta r),$$

where $\Delta\mathbf{x}^{HS}$ is the hard-sphere displacement, and Δr is the interparticle separation after the affine and Brownian displacements. The Heaviside step function is included to ensure that the displacement is only applied to overlapping particle pairs and the coefficient $1/2$ is chosen to return the particles to contact. These displacements are intended to mimic the effects of a hard-sphere interparticle force. Due to the pairwise fashion in which they are applied, however, there are some induced overlaps that cannot be resolved due to three particle effects. As shown by the temporal decay of the stress autocorrelation function, these residual overlaps do not contaminate the hard-sphere behavior.

In the approach of Heyes and Melrose [50], the suspension stress tensor is determined from $\langle\hat{\mathbf{r}}\hat{\mathbf{r}}g(\mathbf{r})\rangle$ at contact over the course of a simulation as a way of determining the contact integral in Eq. (6). This ensures that an equilibrium distribution recovers the theoretical value for the interparticle stress, the osmotic pressure contribution $4\phi g(2a)\mathbf{I}$. We use a different method that involves calculating pairwise interparticle forces, $\mathbf{F}^{P}$, that would result in the hard-sphere displacements in Eq. (21) [52]. In the absence of HI, the force associated with each displacement is given by

$$\mathbf{F}^{P}=6\pi\eta a\frac{\Delta\mathbf{x}^{HS}}{\Delta t}, \tag{22}$$

which is simply the average Stokes drag on the particle over the course of the hard-sphere displacement. The same procedure can be applied with HI and the results match [52].

After the interparticle forces have been calculated, it is straightforward to determine the bulk stress. In the absence of HI, Eq. (5) reduces to

$$\langle\mathbf{\Sigma}\rangle=-\langle p\rangle_{f}\mathbf{I}-nkT\mathbf{I}+2\eta\left(1+\frac{5}{2}\phi\right)\langle\mathbf{E}\rangle-n\langle\mathbf{x}\mathbf{F}^{P}\rangle.$$

With no HI, the Brownian interparticle contribution to the stress is zero, while the hydrodynamic contribution reduces to the dilute-limit Einstein correction to the viscosity, $(5/2)\eta\phi$, which represents a Newtonian rheology. All of the interesting rheological behavior is due to the interparticle force contribution, $n\langle\mathbf{x}\mathbf{F}^{P}\rangle$. For simplicity, only this contribution is presented for the BD stresses.

C. Simulation setup

When the number of particles in the simulation is not specified, the simulations performed here use a cubic periodic box of 512 particles for ASD and 1331 particles for BD. In either case, initial configurations are randomly distributed by a Monte Carlo algorithm (i.e., taken from an equilibrium ensemble). The box is sheared and periodically reset during the simulation and the boundary conditions of Lees and Edwards are used [53]. Recall that the Péclet number is defined $Pe=3\pi\eta\dot{\gamma}a^{3}/kT$; ASD simulations are performed for $0.05\le Pe\le 500$ and BD simulations for $0.5\le Pe\le 500$.

The particle volume fractions studied were $0.30\le\phi\le 0.56$, with most results shown at $\phi=0.40$. For start-up and cessation, most simulations impose shearing until the total

shear strain is $\dot{\gamma}t = \gamma = 5$ before cessation. This generally allows us to probe the complete start-up dynamics, as the systems studied approach steady state by $\gamma = 5$. At this point, the bulk flow is stopped, setting $\mathbf{E} = 0$, and the relaxation under the action of Brownian motion is monitored.

1. Near-equilibrium behavior

To obtain the shear stress autocorrelation function $C_s(t)$ involves simulation at equilibrium ($Pe = 0$) for a long period of time. During this long simulation, three independent stresses for the system are monitored: Σ_{xy}, Σ_{xz}, and Σ_{yz}. The time average of each is zero at equilibrium and fluctuations are measured by the autocorrelation function. Because we are interested in the total suspension stress—and not the individual particle contributions, as is necessary for other correlation functions such as the mean-square displacements—it is straightforward to keep a record of the values of the three shear stresses for all time to maximize the data available to calculate $C_s(t)$. From the data, three separate autocorrelation functions are calculated for fluctuating shear stresses which are simply averaged for calculating $C_s(t)$. Time is nondimensionalized by the diffusive time a^2/D; the dimensionless time step for the BD system is $\Delta t = 2.5 \times 10^{-4}$ while for ASD, the time step is $\Delta t = 10^{-4}$ to ensure a smooth $C_s(t)$ at small times. Simulations are performed at several volume fractions. The systems are large enough to enable study at high densities, including the metastable disordered state above the phase boundary at $\phi \simeq 0.494$. Starting configurations at large ϕ are obtained using a density quenching technique [54,55], and the osmotic pressure was monitored to ensure that crystallization did not occur.

2. Nonequilibrium behavior

When simulating steady shear flow, typically one or a few initial configurations are used. The transient part of the results (from the initial configuration at equilibrium to the steady state) is discarded. In order to reduce statistical noise and get average properties, the simulations are run for a long time and the properties of the suspension are sampled at certain time intervals. At steady state for a constant shear rate, the system is ergodic and thus an average over time is equivalent to one over multiple configurations.

For time-dependent shear flow or during the start-up and cessation of flow, the time dependence is of central interest and a more faithful ensemble averaging is needed. We use many initial configurations, each taken from an equilibrium ensemble (generated by a Monte-Carlo algorithm). For the pair distribution function $g(\mathbf{r})$, ensemble averages are made over $O(1000)$ initial configurations. When only the stresses are needed, $O(100)$ initial configurations are sufficient. We thus start the simulation with an equilibrium configuration and undergo a step increase in the shear rate, or Pe, which is then held constant while the stress response during start-up is monitored. Once the simulations are completed, properties of the suspension are calculated by averaging the results, at every sampled time, over all realizations. The start-up flow is simulated for five particle diffusive time units at $Pe < 1$ and a strain of five ($\dot{\gamma}t = 5$) at $Pe \geq 1$. The flow is then abruptly stopped by no longer including the affine displacements in the evolution equation (21) for five more time units using the same scaling of time. At high shear rates, this continued use of the flow time scale, $\dot{\gamma}^{-1} = (a^2/D)Pe^{-1}$ (much smaller than the diffusion scale a^2/D), provides finer resolution of the immediate postcessation behavior.

Start-up flow and flow cessation are studied using ASD and BD in the same manner, but with a few changes. The time step for all Brownian Dynamics simulations is $\Delta t = 2 \times 10^{-4}$. HI have the effect of slowing down the dynamics of the system, and thus a larger time step ($\Delta t = 4 \times 10^{-4}$) is used except at $Pe \leq 1$ where the time step $\Delta t = 2 \times 10^{-4}$ (in diffusive time units, a^2/D) is taken instead. In ASD, both the affine and hydrodynamic displacements are set to zero upon cessation.

V. SIMULATION RESULTS

Before considering transient behavior, steady shear results for hard-sphere suspensions with HI are presented over a range of Pe at $\phi = 0.4$. The behavior at a similar range of Pe was presented by Foss and Brady [10] for $\phi = 0.45$, but the larger system size computationally accessible now will be shown to yield, at low Pe, qualitatively different observations. This is followed by simulations near equilibrium performed for suspensions with and without HI; the resulting stress autocorrelation function $C_s(t)$ is compared to theoretical predictions from Sec. III B and the infinite frequency elastic modulus G'_∞ is compared to experimental results. Start-up and cessation of shear flow are then presented: We focus on elucidating the different time scales relevant to the structural development and stress evolution.

A. Steady-state shear flow and influence of system size

Suspensions undergoing steady shear flow typically approach a statistically steady state after a few strain units, and the stress then depends only on Pe and ϕ for hard spheres. Foss and Brady [10] presented results of the steady Brownian and hydrodynamic contributions for $0.316 < \phi < 0.49$ to the shear viscosity $\eta^{B/E} = \sigma_{xy}^{B/E}/\eta\dot{\gamma}$, as well as to the first (N_1) and second (N_2) normal stress differences. Figure 1 shows results from our work at $\phi = 0.4$ which agree well with their findings. The total viscosity is shear thinning until $Pe \approx 5$, as the Brownian stress, which dominates for $Pe \ll 1$, saturates at conditions far from equilibrium. At $Pe > 5$, the hydrodynamic viscosity η^E dominates and mild shear thickening is seen with increasing Pe. N_1^B is positive at small Pe, reaches a maximum at $Pe \approx 1$, then saturates (and decreases when normalized with the shear rate) as Pe increases. N_1^E is negative at all Pe and its magnitude increases with the shear rate. The total first normal stress difference N_1 is thus positive at low Pe and negative at high Pe, owing to the transition from Brownian to hydrodynamic dominance as Pe increases. The change of sign in N_1 can also be explained by a change in the microstructure: At small Pe, the positive N_1 results from the buildup of density near the compressional axis without the small carry-over to the extensional axis which must be pulled apart to give a negative N_1. Both the Brownian and hydrodynamic contributions to N_2 are negative at

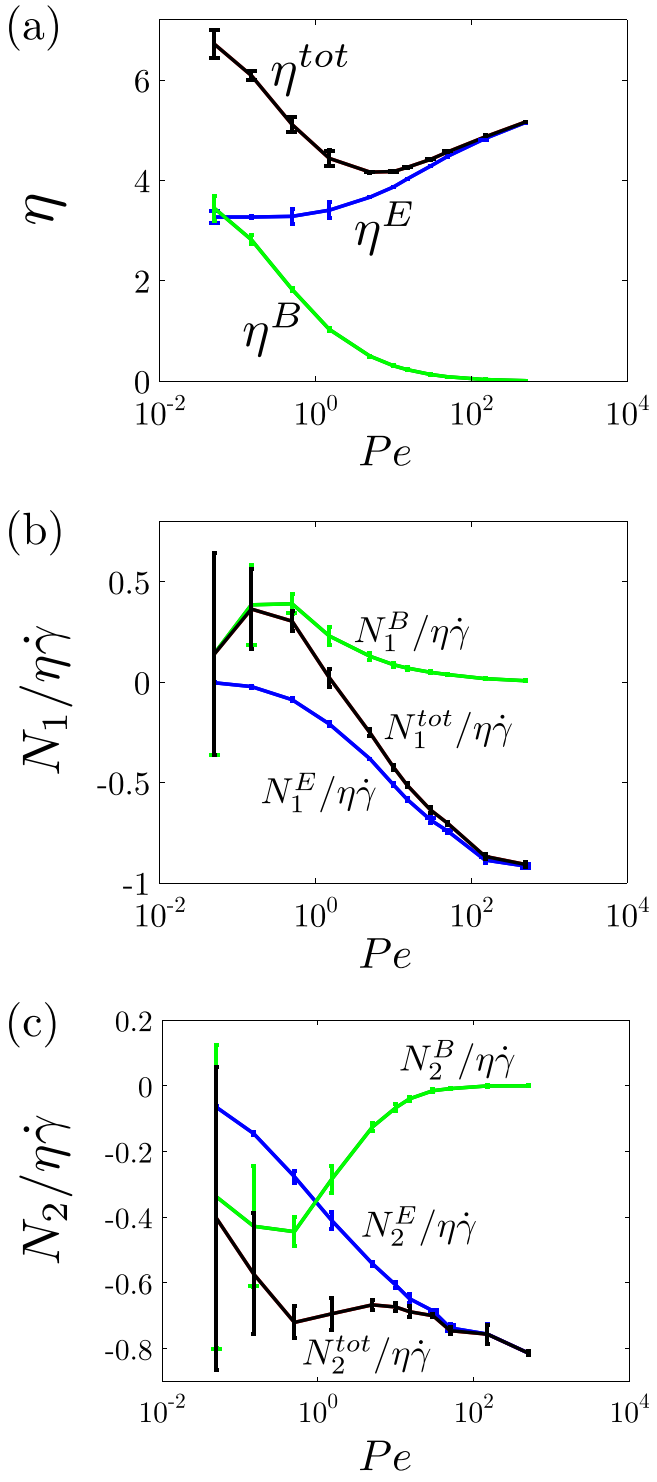

FIG. 1. Steady state values and error bars for the viscosity, first and second normal stress differences at $\phi = 0.4$ with ASD simulations and $N = 512$: Hydrodynamic, Brownian, and total stress.

all Pe. At low Pe, N_2^B shows significant statistical uncertainty. Similar to N_1^B, $|N_2^B|$ is also maximized near $Pe = 1$.

Normal stress differences arise only when the suspension microstructure is anisotropic and thus should vanish for a disordered suspension at equilibrium ($Pe = 0$). Foss and Brady [10] found that $N_1/\eta\dot{\gamma}$ and $N_2/\eta\dot{\gamma}$ in fact grew as $Pe \to 0$, and attributed this pathological result to statistical noise. The flow curves are shown in Fig. 1 because the simulations performed here with more particles in the computational unit cell show this behavior which, although expected, has not been reported in the literature before: Both the Brownian and the hydrodynamic contributions to N_1 and N_2 decrease as Pe approaches 0. Our low Pe results, even for many initial configurations, remain very noisy for N_2^B.

Foss and Brady [10] used the original Stokesian dynamics method, for which the computation time is $O(N^3)$, to compute steady shear results with $N = 27$ particles in the computational unit cell. They reported ordering in the microstructure due to the small box size and noted that this effect decreases when N is $O(100)$ but did not show the change in shear stress with the number of particles in the unit cell and did not use systems larger than $N = 123$. ASD simulations reduce the calculational expense to $O(N \ln N)$ or $O(N^{1.25} \ln N)$, respectively, when computations are without [56] or with [15] Brownian motion. This acceleration of the calculations facilitates use of more particles in simulations. For ASD simulations, we use $N = 512$ and compute $O(1000)$ independent realizations of the same suspension conditions to reduce statistical noise. Reproducing the $\phi = 0.45$ condition of Foss and Brady [10] with both $N = 27$ and $N = 512$ in Figs. 2(a) and 2(b), we see that the results vary strongly with N. For the small system, the shear stresses η^E and η^B both fluctuate nearly periodically. The fluctuations in small systems are also visible in the normal stress differences, and we note that the mean of the normal stress differences is significantly higher for the smaller system size. Short runs at $\phi = 0.4$ with $N = 27$ show similar pseudo-periodic behavior. At high Pe, Figs. 2(c) and 2(d) show that η^E is larger for $N = 27$ than $N = 512$, but the size effect is much weaker than at low Pe where Brownian stress is dominant. At high Pe, the particle interactions close to contact dominate the rheology and the system size becomes less critical. The number of particles used in most of our simulations is $N = 512$. We see that some size dependence is visible when comparing results with $N = 512$ and $N = 3375$ in Figs. 2(c) and 2(d) but the difference is small.

B. Near equilibrium behavior

1. Brownian dynamics

The computed relaxation behavior of equilibrium fluctuations as measured by the shear stress autocorrelation function at various volume fractions is shown in Fig. 3. The decay of $C_s(t)$ with time is strictly monotonic. At short times, $C_s(t)$ appears to diverge as $t^{-1/2}$, in agreement with the theoretical arguments given above. The suspension stress at any instant is either zero or infinite depending on whether or not a particle-particle contact is present. The time average of such a stress profile is finite (in this case, it is zero), but the variance, and thus the zero-time value of C_s, is infinite. This divergent behavior implies that there is no limiting value for the high-frequency elastic modulus, G'_∞. In this work, the "instantaneous" stress from the simulation is actually a time-step-averaged stress, and thus the δ-function nature of the stress is removed. Despite this, $C_s(t)$ still appears divergent at times as short as one time step, $\Delta t = 2.5 \times 10^{-4}$. Examination of shorter times requires smaller time steps, which one can see from Eq. (22) results in larger instantaneous forces and

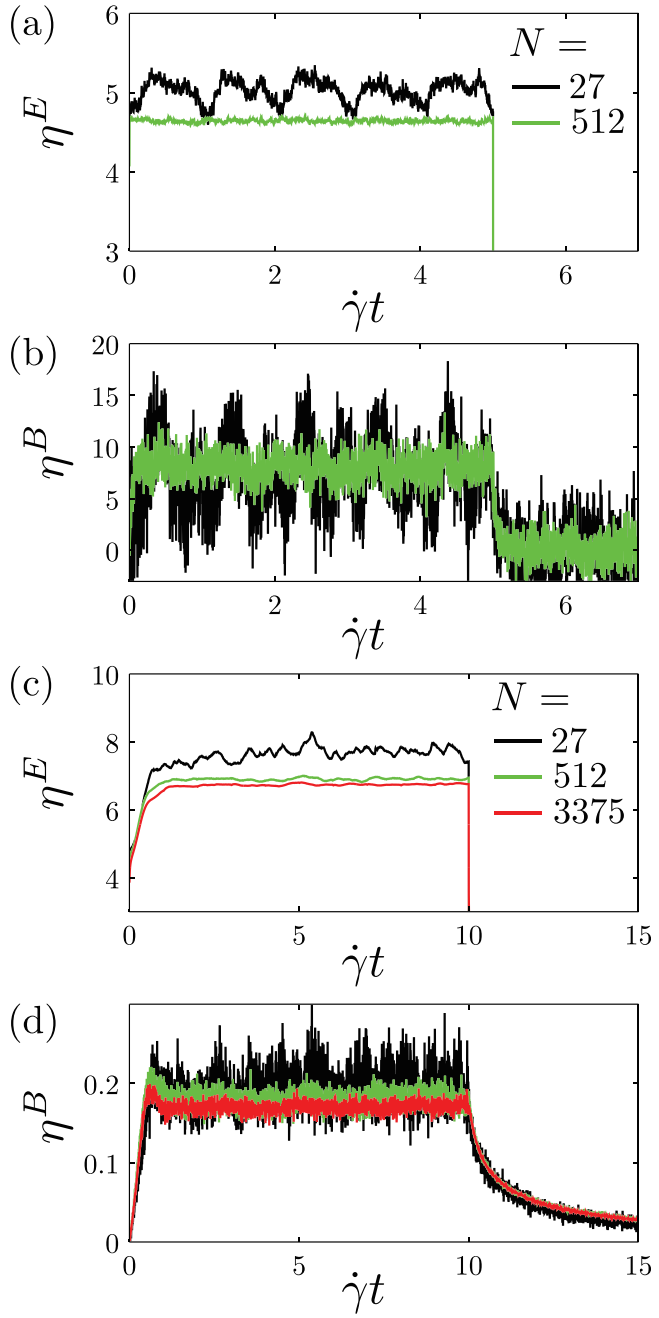

FIG. 2. Time evolution for the Brownian and hydrodynamic shear stress contributions at (a)–(b) $Pe = 0.05$, $\phi = 0.45$ and (c)–(d) $Pe = 50$, $\phi = 0.45$ with ASD simulations. The results are shown for $N = 27$, $N = 512$ and, for $Pe = 50$, $N = 3375$. In comparing the relaxation in figures (b) and (d), note that the time is scaled with the inverse of the shear rate $\dot{\gamma}^{-1}$ so one time unit on (b) corresponds to 1000 time units on (d).

stresses, enabling $C_s(t)$ to increase further at the shorter times being probed. The $t^{-1/2}$ behavior of $C_s(t)$ serves as a good check for the hard-sphere interparticle force algorithm used here, as a soft interparticle potential would result in a finite modulus. The long time behavior of $C_s(t)$ relaxes to zero, but the precise form of the decay is not evident due to statistical noise.

2. Accelerated Stokesian dynamics

Inclusion of HI produces a qualitatively different behavior. Figure 4(a) shows the time-dependent behavior of $C_s(t)$

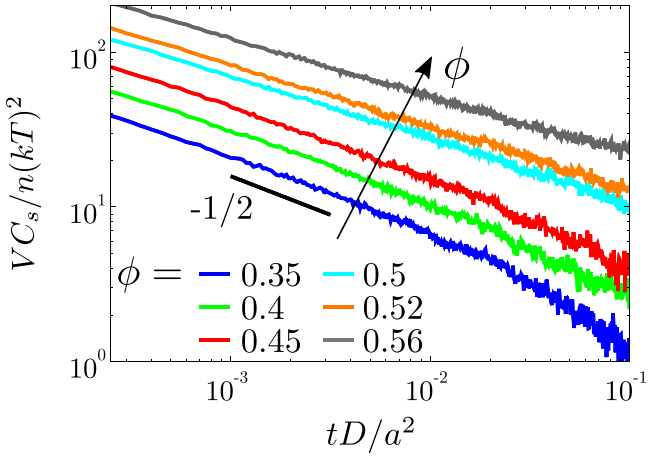

FIG. 3. Shear stress autocorrelation function $C_s(t)$ computed by BD, normalized by $n(kT)^2/V$ with time normalized by a^2/D for several values of volume fraction ϕ.

computed by ASD at various volume fractions. Again, the relaxation is monotonic, but with HI $C_s(t)$ approaches a constant at short times indicative of the existence of a finite high-frequency modulus. The hard-sphere δ-function interparticle force is not needed to keep the particles from overlapping as the strong lubrication interactions between the particles are sufficient. The stress present at equilibrium is no longer the interparticle stress, but the Brownian stress as defined in Eq. (7). This stress does have a finite instantaneous value at each particle configuration. As a consequence, the variance of the stress, and thus G'_∞, is finite. The value of $C_s(t)$ subtracted from its constant zero-time value is shown in Fig. 4(b). The initial decay is linear in time in agreement with the theory discussed in Sec. III B. The precise nature of the long-time decay cannot be extracted from the data due to statistical noise.

The values of the high-frequency modulus G'_∞ from ASD are shown as a function of ϕ in Fig. 5. Also plotted are experimental data on model hard-sphere systems from Shikata and Pearson [58]. Though in fair agreement, the experimental data are consistently larger than the simulation data, a result that may be due to some residual effect of the steric stabilization in these silica dispersions. The stabilizing steric layers keep particles from coming into contact and thus limit the hydrodynamic lubrication interactions, effectively eliminating HI near contact. Without HI the modulus is infinite, and thus at the finite (but high) frequency at which Shikata and Pearson [58] measured G'_∞ one would expect a modulus that is larger than the true hydrodynamic results. The simulation results here are obtained from the zero-time value of the shear-stress autocorrelation function. Alternatively, one could obtain G'_∞ by calculating the variance of the stress associated with numerous independent random configurations without evolving these configurations over time. The theoretical prediction from Swan *et al.* [57] is also plotted in Fig. 5. Their analysis for semidilute colloidal suspensions yields a high-frequency elastic modulus $G'_\infty a^3/kT = 0.19\eta'_\infty g(2,\phi)\phi^2/\eta$. This result follows the same slope as our ASD results but seems to be off by a multiplicative factor.

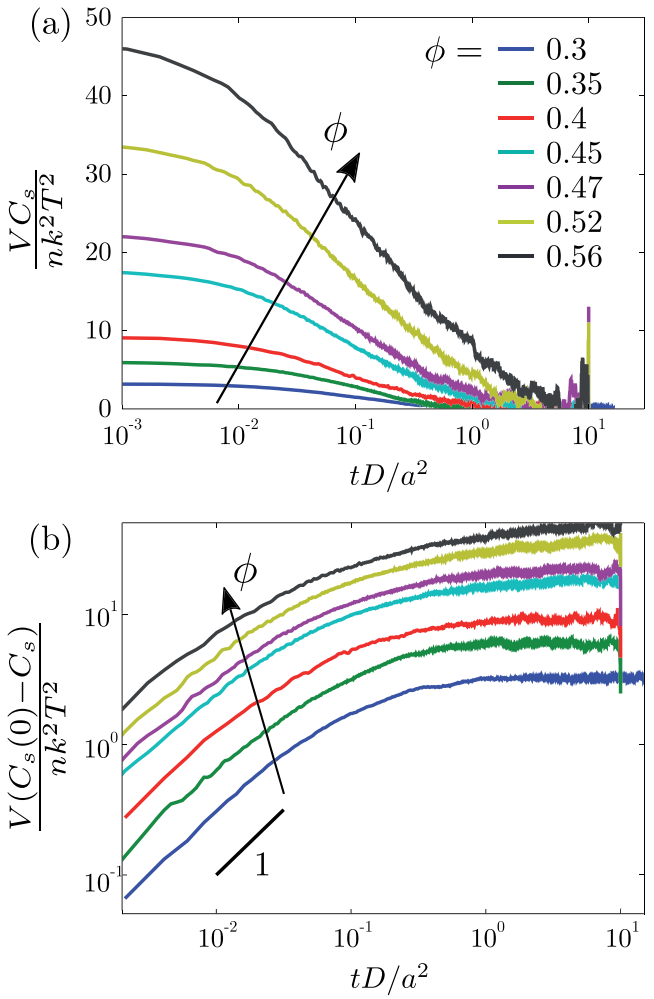

FIG. 4. (a) Shear stress autocorrelation function $C_s(t)$ computed by ASD and normalized by $n(kT)^2/V$ as a function of time, normalized by the diffusive time, a^2/D, for several values of volume fraction ϕ. (b) The same $C_s(t)$ subtracted from its zero-time value to show the initial decay of $C_s(t)$.

C. Start-up and cessation of shear flow

To illustrate the methodology used, we first show the computed viscosity and normal stress differences for a suspension with HI at an intermediate shear rate ($Pe = 10$). We then examine the role of HI by comparing results from BD and ASD, analyzing the time dependence of the viscosity in both cases for start-up and after cessation of the shear flow. Finally, we focus on suspensions with HI to examine the shear stress and normal stress differences and their relations to the evolving particle microstructure in more detail.

A suspension initially at equilibrium is subjected to fixed shear rate until a total strain $\dot{\gamma}t = 5$ such that the stress reaches steady state, and flow is then stopped. After cessation of shear, the evolution of the suspension structure and properties are sampled as a function of time. This is performed for many initial configurations.

During the start-up of shear flow in a suspension with HI for $\phi = 0.4$ and at $Pe = 5$, the total viscosity due to the particle phase undergoes a transient with overshoot, as shown in Fig. 6. Separating the contributions of the hydrodynamic viscosity η^E and the Brownian viscosity η^B shows that the overshoot comes from η^B. Both contributions reach steady state at $\gamma \approx 1.3$. A stress overshoot is also observed experimentally: For start-up of shear flow in dispersions at higher ϕ for low Pe, where η^B dominates, Laurati *et al.* [20], Koumakis *et al.* [19], and Koumakis *et al.* [22] observe overshoots during the transient before reaching steady state. After cessation of flow, η^E decays with the fast inertial relaxation time, $a^2/\nu = \rho a^2/\eta$, where ν is the kinematic viscosity of the solvent. In ASD, the inertial effects are eliminated by setting $Re = 0$ (equivalent to $\rho = 0$) and therefore, the hydrodynamic stresses vanish instantly, as shown in Fig. 6, whereas η^B tends toward zero with a finite relaxation time determined by the structure's diffusive approach to equilibrium.

For $Pe = 5$, N_1 is briefly positive during the start-up of shear flow, when the positive N_1^B contribution dominates, and then becomes negative at steady state [Fig. 7(a)]. The contributions to N_1 require $\dot{\gamma}t \geq 2$ to reach steady-state. After cessation of flow, N_1^E drops instantly to zero and, as a consequence, the first normal stress difference is positive again as the Brownian contribution relaxes to zero. For N_2, both the hydrodynamic and the Brownian contributions are negative [Fig. 7(b)] and both exhibit an overshoot. The steady state is, as for N_1, reached after about a strain of two.

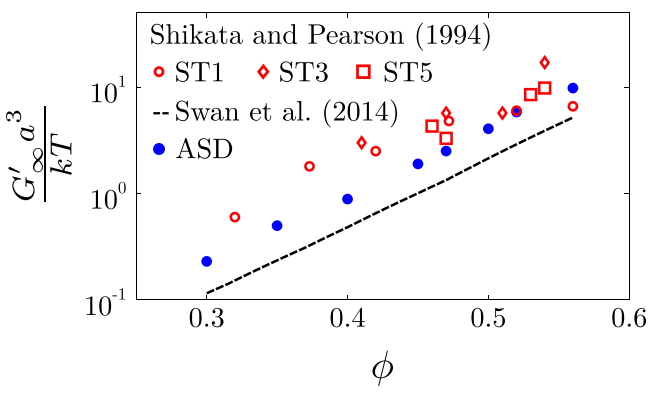

FIG. 5. Comparison of the high-frequency dynamic modulus, G'_∞, scaled by kT/a^3, obtained from ASD (filled circles), with the theoretical prediction (dashed line) of Swan *et al.* [57] and experimental results (open symbols) of Shikata and Pearson [58]: ST1, ST3, and ST5 are approximately monodisperse spherical silica particles of three different sizes.

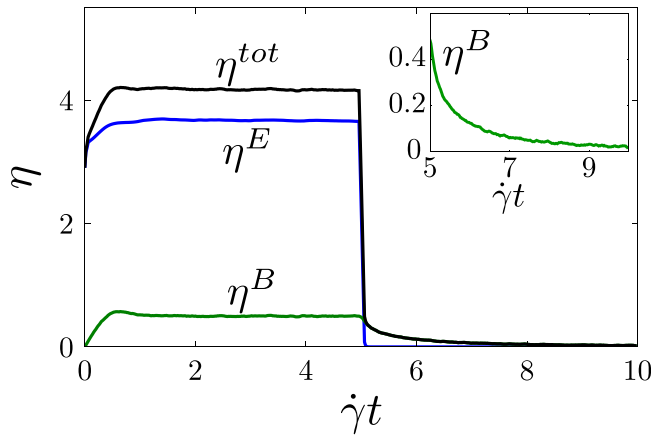

FIG. 6. Evolution of the viscosity components during the start-up and cessation of shear flow for $\phi = 0.4$ at $Pe = 5$ from ASD simulations using $N = 512$ particles. The inset is a magnified view of the relaxation of the Brownian contribution.

After cessation of flow, it is interesting to note that N_2^B relaxes to zero much more rapidly than N_1^B.

1. Comparison: Suspensions with and without HI

a. BD—Start-up. Figure 8(a) shows the instantaneous stress during start-up of flow at several Pe from BD at $\phi = 0.45$. Figure 8(a) shows that plotting the viscosity as a function of time scaled diffusively, by a^2/D, roughly collapses the data for small Pe. The viscosity is seen to grow as $t^{1/2}$ at short times as predicted by the theory in Sec. III B. At longer times, shear thinning behavior is seen, as the curves take on steady state values that decrease with Pe.

Also plotted in Fig. 8(a) is the time integral of $C_s(t)$, obtained by performing the integral in Eq. (9) at zero frequency with t (rather than ∞) used as the upper limit of integration. At short times, this integral increases as $t^{1/2}$, corresponding to the $t^{-1/2}$ behavior of $C_s(t)$; at long times the integral asymptotes to the zero shear viscosity η_0. The good agreement of the transient stress integral at very low Pe is expected as the response to a change in $\dot\gamma$ is indistinguishable from an equilibrium fluctuation.

At high Pe the behavior deviates from the near equilibrium case, particularly at long times. There is still a discernible $t^{1/2}$ growth at short times in the viscosity for all Pe, but the slope of the curves increases with Pe in Fig. 8(a). This indicates that the characteristic time is changing to a smaller time scale, perhaps to the flow time $\dot\gamma^{-1}$ although the data do not allow a conclusive statement. The $t^{1/2}$ behavior does not persist for long times at high Pe and the growth shifts to be nearly linear, as is more clearly seen in Fig. 8(b), which shows the same data with time normalized by $\dot\gamma^{-1}$. The initial $t^{1/2}$ behavior can only be seen at very small times for high Pe, and is manifested by infinite slope at zero time. Viscosities for all Pe reach a plateau value in unit strain, in agreement with the theoretical development in Sec. III C that shows the structure during start-up flow reaches steady-state exponentially on the time scale of $\dot\gamma^{-1}$; see Eq. (17). There appears to be a small overshoot in the viscosity with time at the higher shear rates. This is apparently an effect of many-body interactions at high ϕ, as such nonmonotonic behavior is absent from the two-body analysis presented in Sec. III C. One also notes from the data that the response to start-up flow becomes independent of Pe at the highest shear rates. The curves for the three highest Pe are all coincident when plotted as a function of strain $\dot\gamma t$. This is consistent with the predictions for the high-Pe asymptotic limit in Eq. (17) [8], as the boundary layer structure becomes well-developed and its influence on the rheology saturates.

b. ASD—Start-up. Figure 9(a) shows that the evolution of the hydrodynamic viscosity during start-up of shear flow

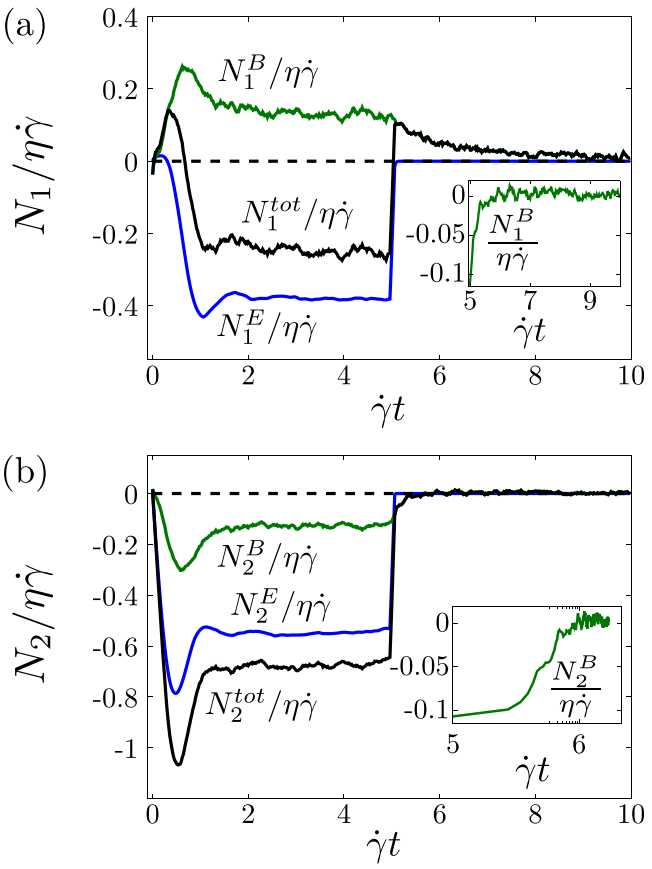

FIG. 7. Evolution of the (a) first and (b) second normal stress differences, showing the Brownian (B) and shear-driven (E) contributions, during start-up and cessation of flow for $\phi = 0.4$ and $Pe = 5$ computed by ASD simulations with $N = 512$ particles. After cessation of flow at $\dot\gamma t = 5$, only the Brownian stress contributes. On the right, the inset shows a closer view of the rapid relaxation of the Brownian second normal stress difference.

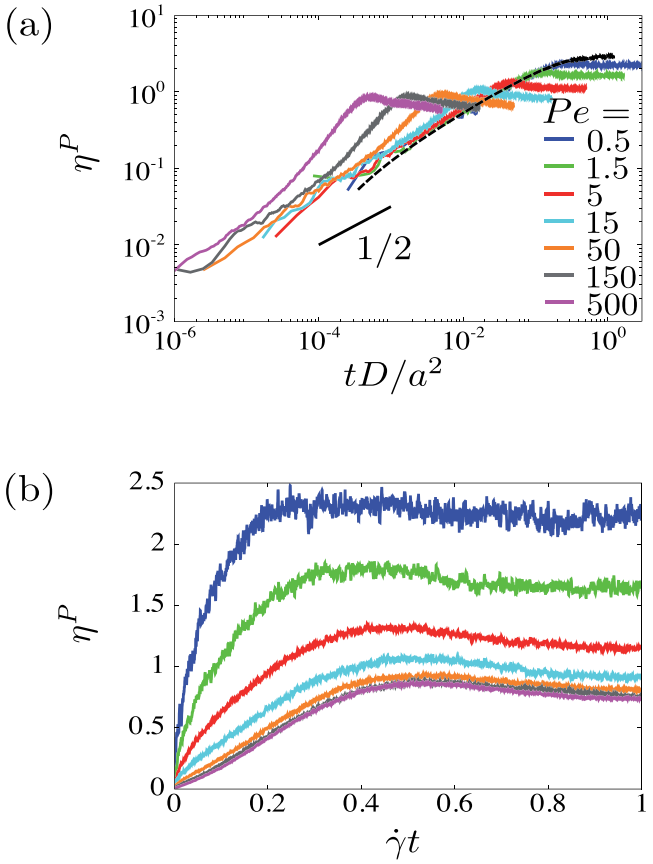

FIG. 8. Start-up flow: (a) Particle viscosity $\eta^P = \sigma_{xy}/\eta\dot\gamma$ as a function of time scaled diffusively, tD/a^2, at several Pe computed by BD at $\phi = 0.45$ and prediction from the autocorrelation function $C_s(t)$ (dashed line). (b) Particle viscosity as a function of strain $\dot\gamma t$ at the same conditions.

from ASD simulations is faster than linear with strain. To facilitate visualization of the short-time evolution, we use a logarithmic time scale and subtract the zero-shear value of the viscosity. The low-Pe viscosities do not depart significantly from their zero-time value, and $Pe = 0.5$ seems to be the lower limit for shear-thickening, as a slight initial increase is seen at this Pe value before the viscosity levels off at a value still close to the zero-time value of the viscosity. Figure 9(b) shows how the Brownian viscosity η^B evolves during start-up for different Pe. The time is scaled diffusively (tD/a^2). The initial slopes of the stress are indistinguishable and show linear growth of η^B with $\dot{\gamma}t$ at all Pe. The prediction from Green-Kubo theory shown in this figure is calculated using Eq. (10) at zero frequency ($\omega = 0$), by replacing ∞ by t in the integral. The linear growth of η^B at short times can be related to the high-frequency behavior at equilibrium. The slower growth of the hydrodynamic viscosity compared to the Brownian viscosity indicates a weaker sensitivity of η^E to changes in the microstructure, as is evident by the fact that it is constant at η'_∞ during small amplitude oscillatory shear. Also, in steady shear flow, the hydrodynamic viscosity is constant at low shear rates and shear thickening is not noticeable below $Pe \approx 1$. Behavior at short times is not unlike behavior near equilibrium and the Brownian viscosity may thus react earlier to start-up flow.

For the Brownian viscosity shown in Fig. 9(b), the curves at $Pe = 0.05$ and $Pe = 0.15$ are superposed and have near-equilibrium behavior. The higher shear rate curves depart from this curve to reach their steady state value: This departure is earliest for the highest Pe. As the hydrodynamic stress is roughly proportional to the shear rate and the Brownian stress saturates for increasing shear rates at $Pe > 1$, the total stress in the suspension is shear thinning. This point can be somewhat physically misleading because the Brownian stress results from structural distortion and the resulting statistical tendency of Brownian motion is to return the structure to equilibrium. As the structure at large Pe becomes strongly anisotropic, the Brownian stress contribution associated with relaxation toward equilibrium saturates while the shear rate continues to increase, and thus the Brownian viscosity (Brownian stress normalized by $\eta\dot{\gamma}$) shear thins.

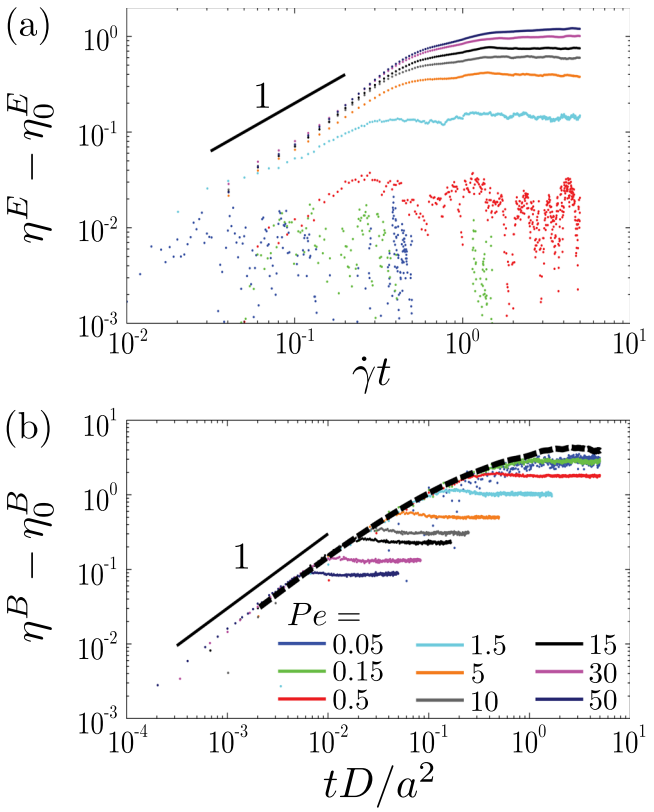

FIG. 9. The (a) hydrodynamic and (b) Brownian viscosity during start-up of steady shear flow simulated by ASD with $N = 512$ for $\phi = 0.4$ at different Pe. The black dashed line in figure (b) is the Green-Kubo prediction of the Brownian viscosity.

We can compare the viscosity from BD in Fig. 8 and the hydrodynamic and Brownian viscosities from ASD in Fig. 9(a). At $Pe < 5$, when the Brownian viscosity is $O(1)$ in ASD and the resulting microstructure is close to equilibrium, the transient behavior of the viscosity from BD and the Brownian viscosity from ASD are very similar and the steady state values are close. There are strong discrepancies at larger Pe, however. In this regime, for suspensions with hydrodynamics as modeled by ASD, the hydrodynamic viscosity dominates and increases faster than the shear rate, resulting in mild shear thickening. The Brownian viscosity becomes negligible at very high Pe. BD simulation does not capture the shear thickening effect at high Pe, exhibiting only shear thinning.

c. BD—Cessation. The flow is abruptly stopped at $\dot{\gamma}t = 5$ and the shear stress is monitored as the structure relaxes by Brownian motion. Figure 10(a) shows the stress as a function of time after cessation from flows at several Pe. We scale stress by the shear-rate independent $kT/(6\pi a^3) = D\eta/a^2$ in order to measure the degree of deformation of the microstructure. Because of this scaling, the stress at the moment of cessation scales as Pe as all the precessation viscosities are of the same order of magnitude. After an initial decay, all relaxation curves coincide at sufficiently long time. It is expected that complete relaxation to equilibrium from any configuration should take place on an $O(a^2/D)$ time, as particles need to diffuse a length on order of their size to fully relax the flow-induced distortion of the microstructure. Figure 10(a) makes a stronger statement, however, showing that each nonequilibrium microstructure takes the same relaxation path toward equilibrium. At intermediate times, a region of $t^{-1/2}$ decay is evident from the simulation data. The precise nature of the stronger terminal decay is not evident due to statistical noise present and small magnitudes of the shear stress.

Figure 10(b) more closely examines the behavior immediately following cessation of the flow. Here, we normalize each stress by its precessation value $\sigma_{xy}(t_{\text{stop}})$. Using this scaling is more appropriate for the short time behavior as the viscosities before the flow is stopped are roughly equal. Time has been nondimensionalized by the time necessary for a particle to diffuse the width of the boundary layer, $\delta^2/D = (a^2/D)Pe^{-2}$, as this is the relevant time scale for the initial relaxation. The theoretical prediction (18) is also shown in Fig. 10(b), where we use $\gamma_r = -1/2$, as this is the value near the compressional axis and we have matched $g_{ss}(0)$ to the precessation value of the viscosity. Excellent

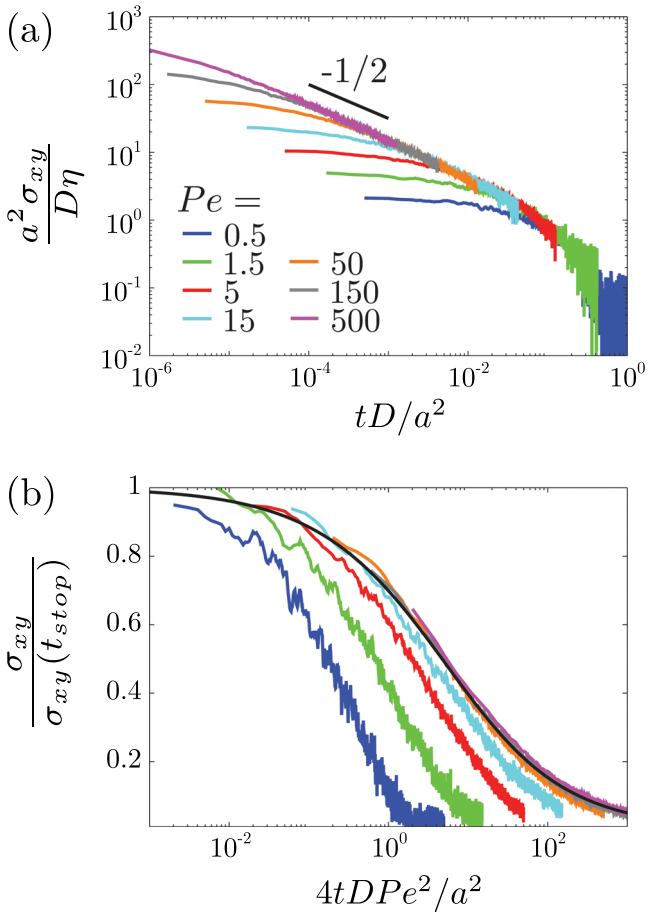

FIG. 10. Flow cessation. (a) Instantaneous suspension stress scaled by $D\eta/a^2$ as a function of time scaled by a^2/D for the BD system at $\phi = 0.45$ and different Pe. (b) Instantaneous suspension stress scaled by its precessation value $\sigma_{xy}(t_{stop})$ as a function of time scaled with the boundary layer length scale, i.e., by $\delta^2/D = (a^2/D)/Pe^2$, at various values of Pe for the BD system at $\phi = 0.45$. The solid curve is the theoretical result (18) using $\gamma_r = -1/2$, its value on the compressive axis, and fitting $g_{ss}(0)$ to the precessation value.

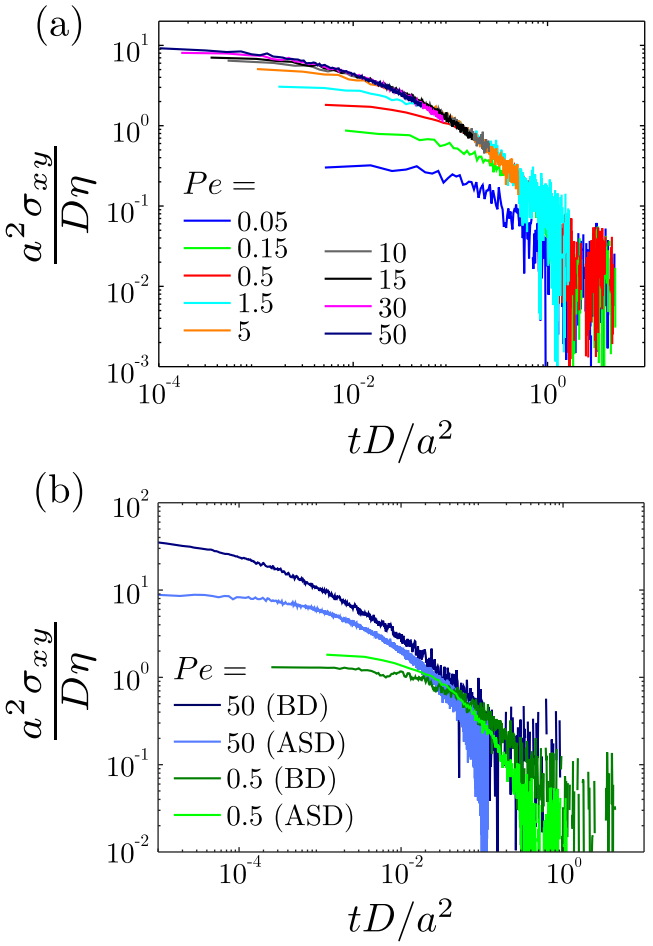

FIG. 11. (a) Brownian stress from ASD at $\phi = 0.4$ during the relaxation after cessation of shear flow for different Pe; (b) comparison of the Brownian stress from ASD at $\phi = 0.4$ and the stress from BD at $\phi = 0.4$ after cessation of weak ($Pe = 0.5$) and strong ($Pe = 50$) shear flow. In (b), for the results from ASD simulations, the self-diffusivity $D^s(\phi)$ has been used to scale the time.

agreement is found between simulation data for $Pe \geq 15$ where the high-Pe boundary layer analysis is more appropriate. The $t^{-1/2}$ decay present at intermediate times in Fig. 10(a) is present here at long times, because time has been scaled differently using the relevant length scale for the boundary layer. Relaxation behavior from lower Pe show some deviation from the theory at long times, but only after the stress has dropped by an order of magnitude. The theoretical boundary-layer solution is only expected to be valid in the high-Pe limit and at low Pe we may be observing a transition to the terminal behavior involving relaxation of larger scale anisotropy of the microstructure outside the boundary layer.

d. ASD—Cessation. Figure 11(a) shows the relaxation of the Brownian shear stresses following cessation at different Pe. Using the diffusive a^2/D time scale, the stresses collapse during the relaxation, as was found for the shear stress from BD. We compare the relaxation of the shear stress from BD and ASD at the same volume fraction $\phi = 0.4$ in Fig. 11(b). For ASD simulations, the time has been scaled with the self-diffusivity $D^s(\phi) = D/\eta'_\infty$ [32] to take the change in diffusivity with concentration for suspensions with hydrodynamics into account. Foss and Brady [10] give the value of the high-frequency dynamic viscosity $\eta'_\infty/\eta = 4.28$ at the volume fraction $\phi = 0.4$. At $Pe = 0.5$, the Brownian shear stress from ASD is higher than the shear stress from BD initially and the curves cross over during the relaxation. At $Pe = 50$, the residual shear stress in the suspension without hydrodynamics is higher than the residual stress coming from the Brownian contribution to the shear stress in the suspension with hydrodynamics (the hydrodynamic stress, which is much larger, vanishes upon cessation of the shear flow). The stress from ASD has a slower relaxation, however, and the curves coincide at the end of the relaxation.

2. Suspensions with hydrodynamics: Stress, cage dynamics, and structure

We consider the general behavior of suspensions with full HI using ASD. As shown in Fig. 12, at zero time, the hydrodynamic viscosity η^E is nonzero and equal to the high-frequency dynamic viscosity η'_∞. The values of $\eta'_\infty/\eta \approx 3.28$ shown here agree with those obtained from time averages of extended steady-shear simulations performed at or near equilibrium (those include the solvent contribution to

the high-frequency viscosity, so $\eta'_\infty/\eta \approx 4.28$) [10,56]. At steady state, the low Pe viscosity remains close to this value of η'_∞. At higher Pe, the hydrodynamic viscosity grows during start-up to plateau at progressively larger values with increasing Pe due to hydrodynamic shear thickening. The η^E curves of Fig. 12(a) do not exhibit stress overshoots, but we do observe regular oscillations during the transient before reaching steady state and at steady state around the plateau value. The strain (i.e., $\dot\gamma t$) needed to reach steady state increases with Pe. For N_1^E, shown in Fig. 12(b), there is a small positive overshoot just at the onset of shearing, and this overshoot is larger for higher Pe. This change of sign at small strains is due to increased probability of particles near the compressional axis, leading to a positive N_1, before the carry-over into the extensional quadrant leads to $N_1 < 0$. The subsequent negative slope of N_1^E during the transient is almost identical at all Pe. There is a negative overshoot for $Pe > 1$ before N_1^E reaches its steady value. The hydrodynamic second normal stress difference N_2^E has essentially identical initial slope with respect to $\dot\gamma t$ (strain) for all Pe during the start-up of shear flow [Fig. 12(c)]. The negative overshoots occur at increasing strain as Pe increases.

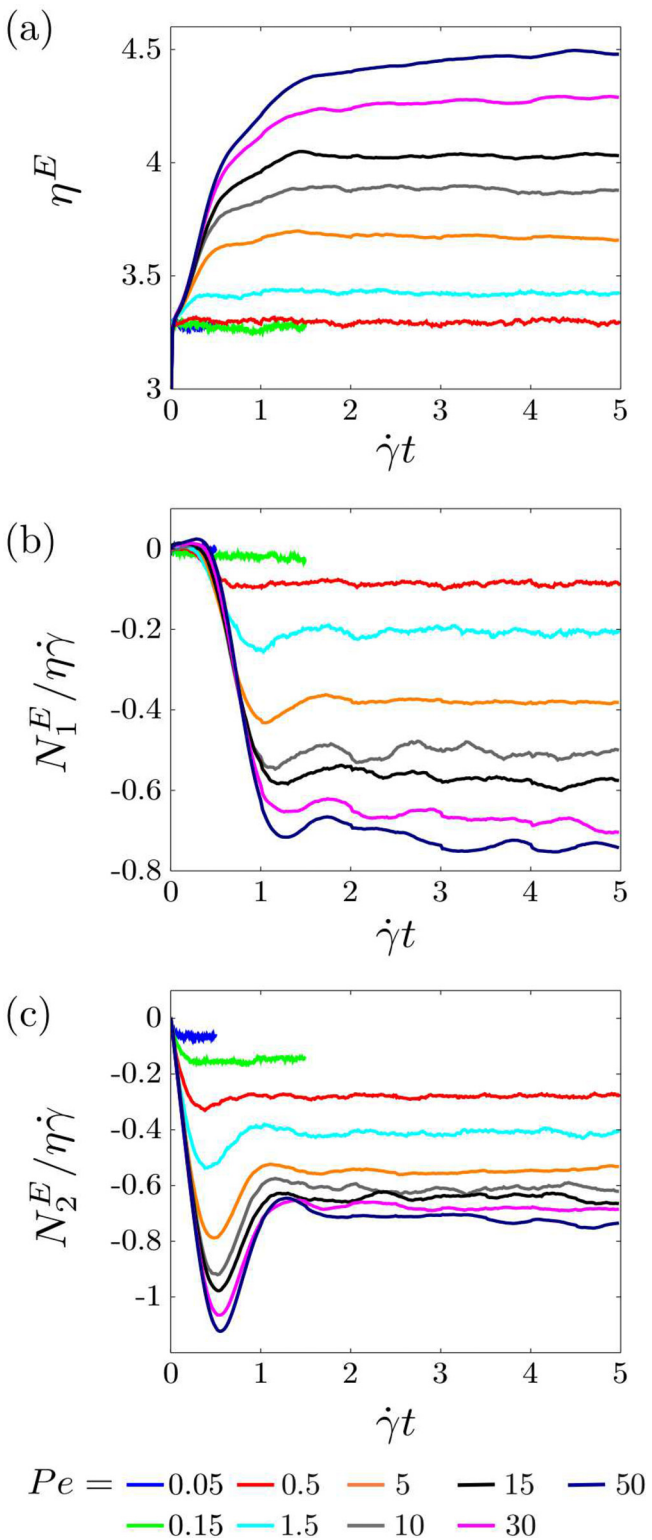

FIG. 12. The hydrodynamic viscosity η^E, $N_1^E/\eta\dot\gamma$, and $N_2^E/\eta\dot\gamma$ during the start-up of shear flow at $\phi = 0.4$ for different Pe from ASD simulations using $N = 512$ particles.

To clarify the point regarding the increase of Brownian stress with increasing Pe, instead of scaling the stress hydrodynamically as $\eta^B = \sigma^B_{xy}/\eta\dot\gamma$, we can scale σ^B_{xy} with the thermal energy to see the increase in stress: $a^2\sigma^B_{xy}/D\eta$. As shown in Fig. 13(a), the Brownian stress overshoots and the strain at which the overshoot occurs depends on Pe. After cessation, the initial relaxation of the microstructure is fast and has decaying exponential form before slowing to an apparently algebraic decay. We find that the behavior can be approximated with a stretched exponential of the Kohlrausch-Williams-Watts functional form [23]: $f(t) = f_{ss}\exp(-(t/\tau)^\beta)$. The parameters β and τ decrease for increasing Pe: For $Pe = 1$, $\tau \approx 0.2$ and $\beta \approx 0.8$; for $Pe = 10$, $\tau \approx 0.06$ and $\beta \approx 0.6$; for $Pe = 100$, $\tau \approx 0.01$ and $\beta \approx 0.3$. The total relaxation time for all Pe is expected to be around $ta^2/D = O(1)$, as the particles need to diffuse at most about a particle diameter to recover the equilibrium configuration with wake closure the reorganization process with the largest length scale. Figure 11(a) also shows the collapse of the Brownian shear stress after cessation when the time is scaled diffusively, but the linear scale used in Fig. 13(b) serves to highlight how rapidly the collapse occurs for high Pe. To understand this behavior, we can picture the distortion from equilibrium of the microstructure as an addition of anisotropy layers: Each increment in Pe (over decades of Pe) adds a layer of anisotropy. When a suspension initially at high Pe ceases to flow, all layers start relaxing at the same time but the highest shear rate layers have the shortest relaxation times and disappear first. Eventually, all the decaying Brownian stresses collapse to a terminal relaxation curve and follow the same path on the diffusive a^2/D time scale.

Figure 14 shows the evolution of N_1^B (scaled thermally) at different Pe during the start-up and cessation of shear flow. During the start-up of shear flow [Fig. 14(a)], there is an overshoot at all $Pe \geq 0.5$. The magnitude of the overshoot and the strain at which it occurs both increase with Pe. The initial relaxation of N_1^B after cessation of shear flow, shown in Fig. 14(b), is slower than that of σ^B_{xy}.

Figure 15(a) shows the evolution of N_2^B during the start-up of shear flow. At each Pe, the magnitude of the overshoots in N_1^B and N_2^B are similar. For N_2^B, the steady value has a nonmonotonic evolution with Pe: It increases until $Pe \approx 15$, then decreases with further increase of Pe. For low

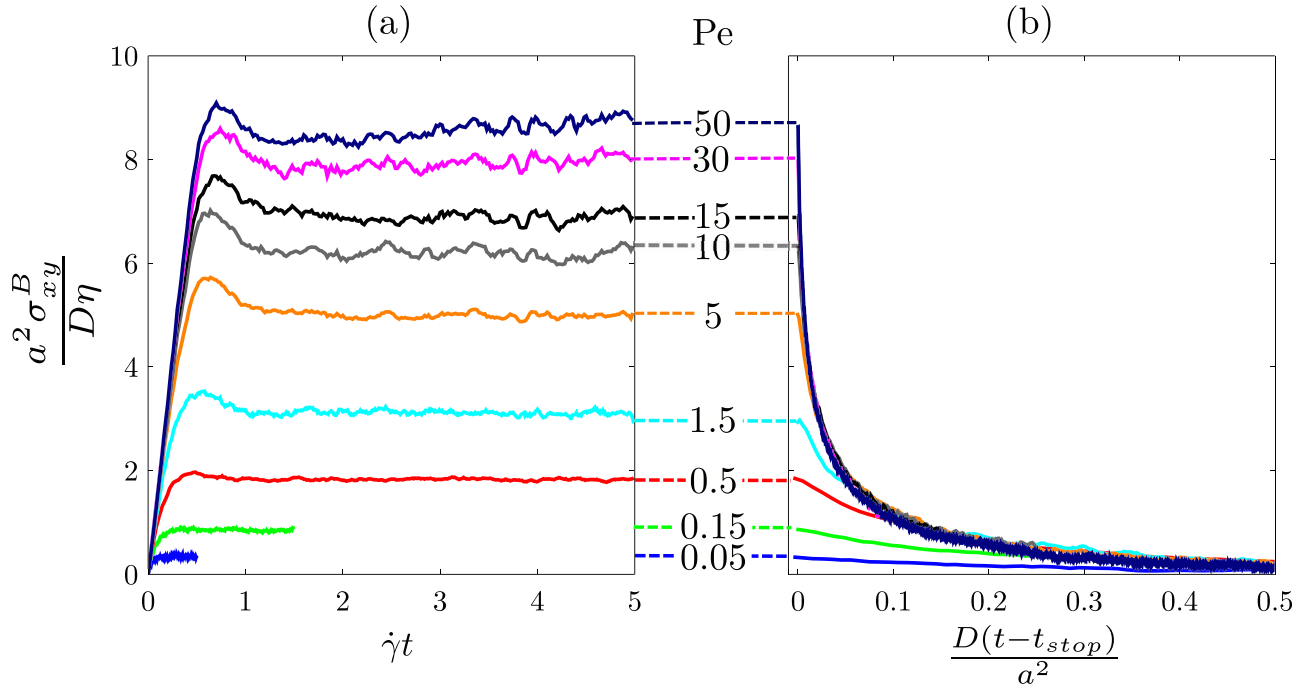

FIG. 13. The Brownian shear stress (a) during start-up and (b) after cessation of shear flow at $\phi = 0.4$ for different Pe for ASD simulations with $N = 512$.

Pe forcing [$Pe \leq 0.5$ in Fig. 15(b)], the relaxation of N_2^B is slow and does not show a change of sign. After cessation of shear flow at high Pe [$Pe \geq 1.5$ in Figs. 15(b) and 15(c)], N_2^B has a fast initial relaxation, then changes sign to a small positive value which decays slowly to zero.

a. Escape from the neighbor cage in freely flowing suspensions. The physical interpretation used to understand the behavior of quiescent glassy suspensions is that particles are able to move locally but are trapped in a cage formed by their neighbors [59–61]. Particles escape this cage due to thermal fluctuations, but the energy barrier to do so becomes higher with increasing concentration. Under shear, glassy suspensions start yielding when the cage of neighbors is broken by the shear flow [19–21]. The same picture is found to be suitable for the moderately concentrated suspensions studied here, despite the fact that particles have far more mobility than in the glassy state. Two arguments can be made to support this claim based on the evolution of the Brownian shear stress during start-up of shear flow: One is related to its

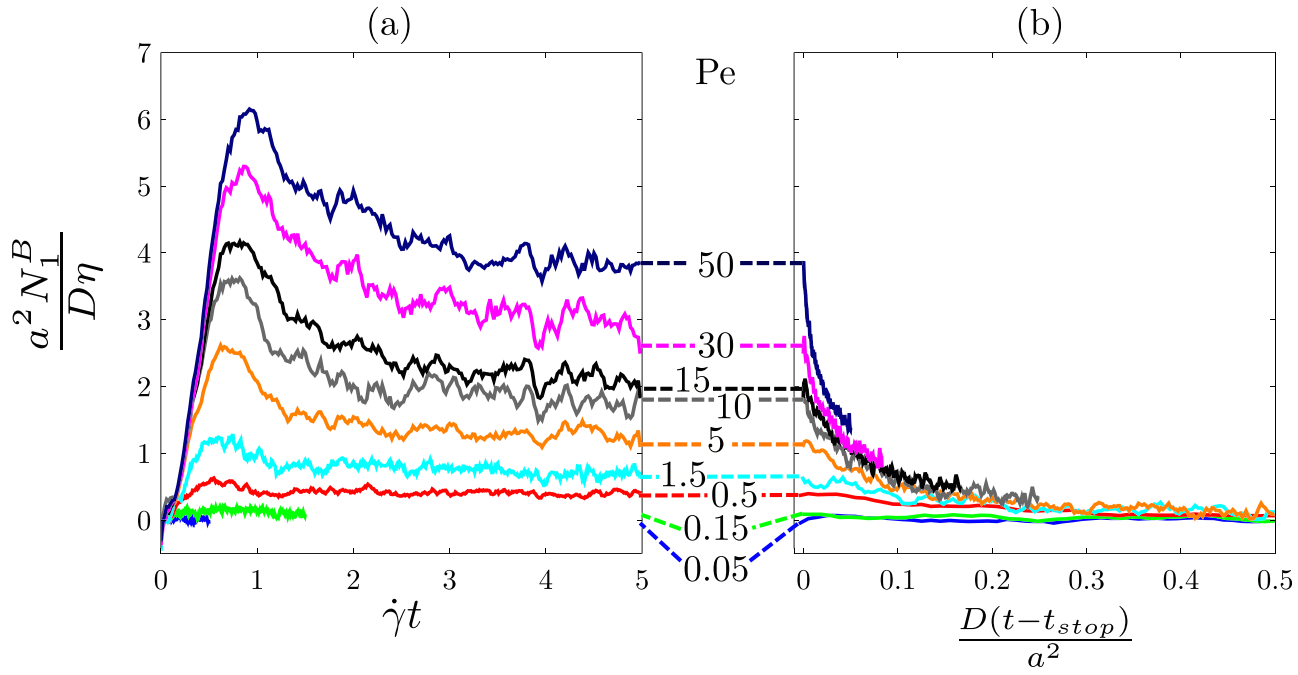

FIG. 14. The Brownian first normal stress difference N_1^B (a) during start-up and (b) after cessation of shear flow at $\phi = 0.4$ for different Pe for ASD simulations with $N = 512$.

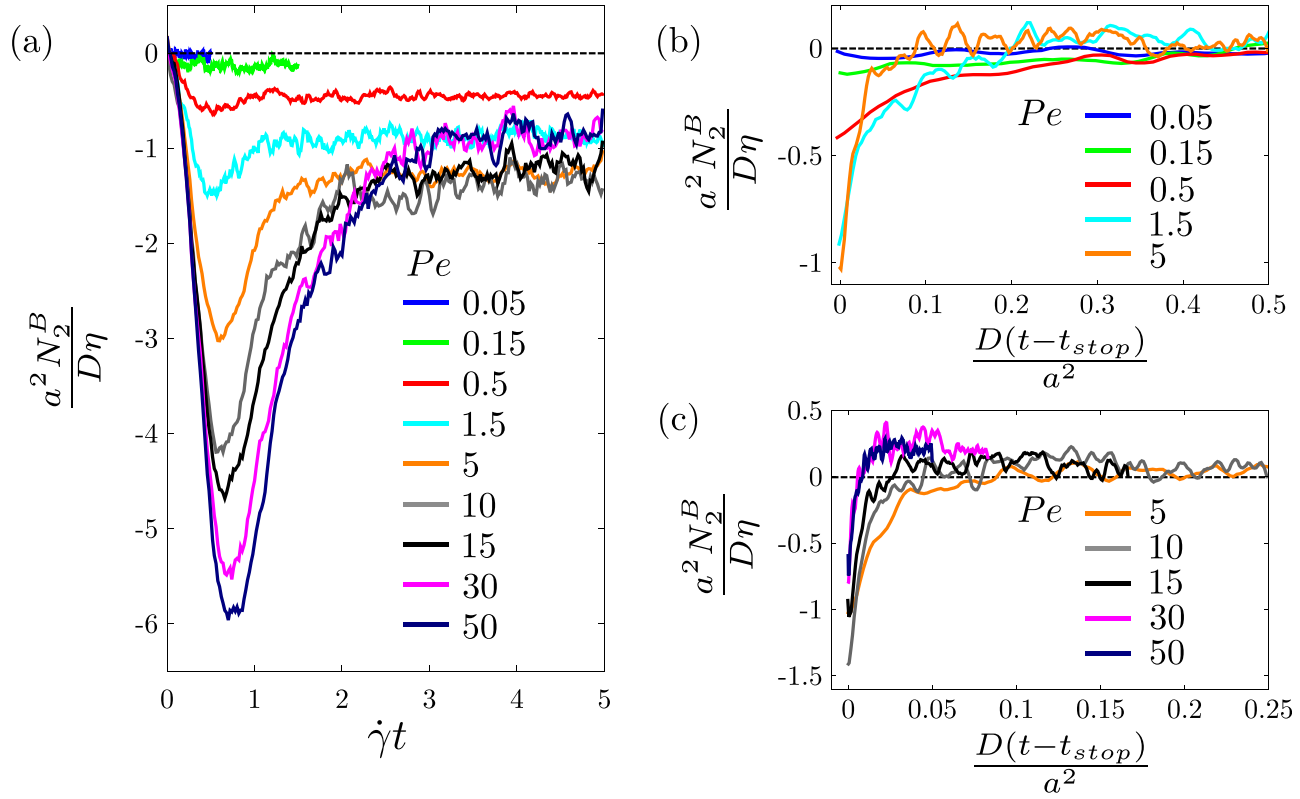

FIG. 15. The Brownian second normal stress difference N_2^B (a) during start-up and (b) and (c) after cessation of shear flow at $\phi = 0.4$ for different Pe for ASD simulations with $N = 512$ particles. The relaxation of N_2^B has been separated into two plots to clarify the difference between the behavior after (b) weak and (c) strong shear flow.

initial slope and the other to the overshoot observable before reaching steady state.

When shear flow is imposed on a suspension, the deformation of the neighbor cage around a given particle is initially affine. During this affine deformation, the Brownian stress is due to the elasticity of the neighbor cage and follows $a^2\sigma/D\eta = 6\pi a^3\sigma/kT = 6\pi(a^3G'/kT)\gamma$, as shown in Fig. 16 for different concentrations. The value of the storage modulus G' is obtained from a Green-Kubo relation in Sec. V B and characterizes the linear, near-equilibrium regime. The shear stress follows this linear slope until $\gamma \approx 0.5$ for $Pe = 100$ at $\phi = 0.4$ whereas for higher concentrations, rapid shearing leads to a deviation of the start-up slope above the elastic modulus calculated at $Pe = 0$. The shear rate needed to drive this slope above G' decreases with increasing concentration.

The second indication that the particles are indeed escaping a cage of neighbors is the occurrence of an overshoot in the Brownian shear stress during the start-up of shear flow: The equilibrium structure is irreversibly broken by the shear

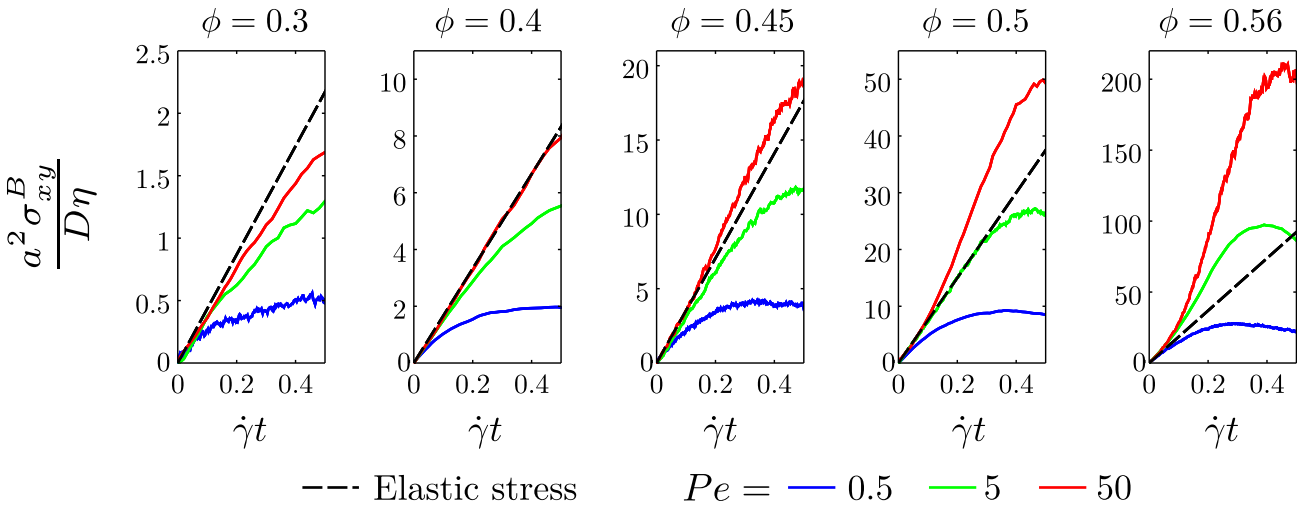

FIG. 16. Brownian shear stress during start-up for different concentrations at $Pe = 0.5$, $Pe = 5$, and $Pe = 50$. The dotted line is the elastic stress calculated with the storage modulus G' obtained in Sec. V B (see Fig. 5).

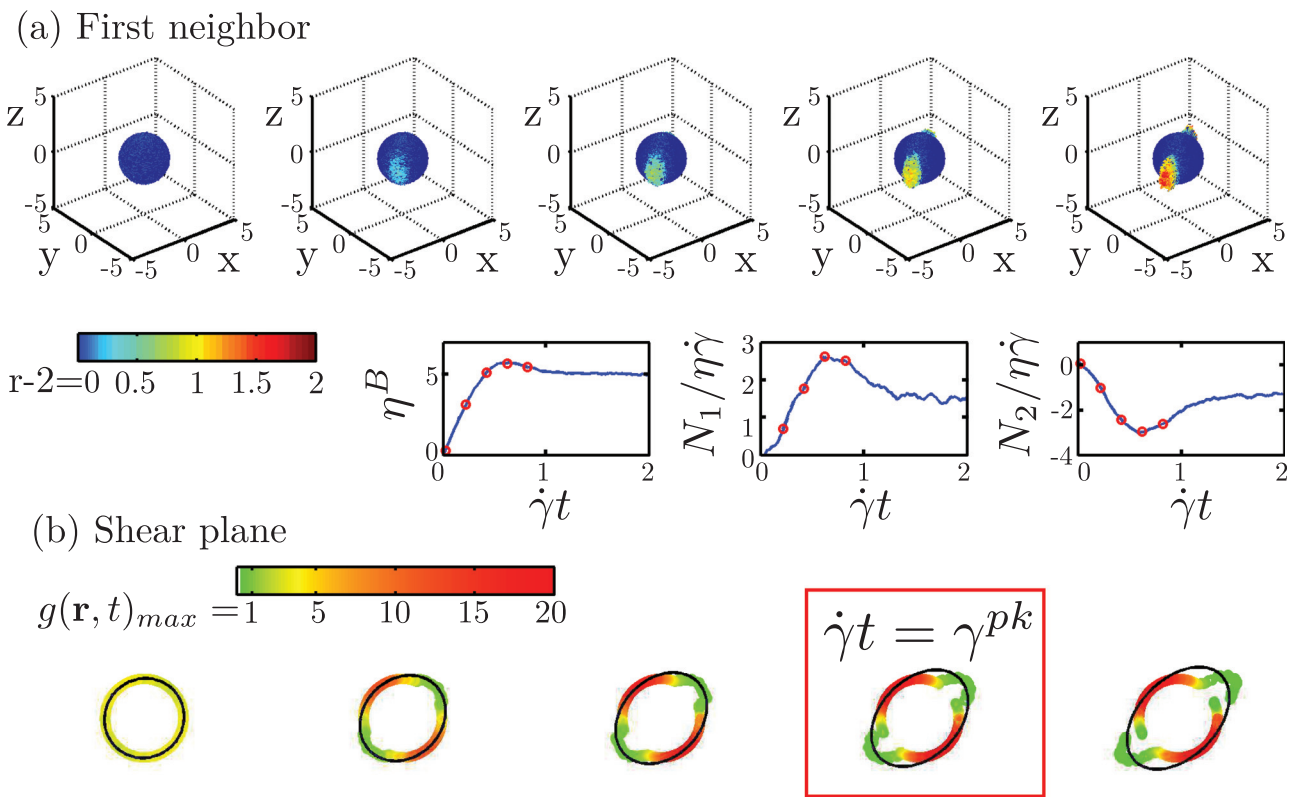

FIG. 17. The deformation and rupture of the cage formed by the first neighbor peak at $\phi = 0.4$ and $Pe = 5$. The three-dimensional view is shown in (a). The change in color corresponds to the distance of the first neighbor from contact. The location of the first neighbor peak in the shear plane at the same times is shown in (b). The color corresponds to the magnitude of $g(\mathrm{r}, t)$ at the peak. The stress overshoot and cage breaking occurs at the fourth image from left in the sequence. The corresponding stress evolution is shown for the Brownian viscosity and first and second normal stress differences. The black ellipse is an estimation of the cage deformation: Its short axis is twice the radius of the particle and its long axis is twice the sum of the particle radius and the cage deformation $2(1 + \sqrt{Pe/\dot{\gamma}t} + \dot{\gamma}t)$ and it is tilted at an angle $\pi/4$.

flow and the stress overshoots in the Brownian shear stress and both normal stress differences (Fig. 17). Because the shear forcing drives the particles toward an anisotropic microstructure while thermal motion resists that deformation and drives the suspension configuration toward equilibrium, the microstructure needed to achieve a balance between these forces depends on Pe. This balance also determines the strain at which the neighbor cage is broken and the stress overshoot occurs. The total deformation of the cage before it breaks is not only due to the shear flow $\dot{\gamma}t$ but also to the diffusive motion $\sqrt{\dot{\gamma}t/Pe}$. The total shear strain before the "escape," γ^{escape}, from the neighbor cage depends on ϕ and is near unity

$$\sqrt{Pe/\dot{\gamma}t} + \dot{\gamma}t = \sqrt{\gamma^{pk}/Pe} + \gamma^{pk} = \gamma^{\text{escape}}(\phi) \approx 1. \qquad (23)$$

$\gamma^{\text{escape}}(\phi)$ is the deformation needed to break the particle cage in the absence of Brownian motion. This limiting value is difficult to determine: As $Pe \to \infty$, the Brownian stress signal-to-noise ratio becomes small and the overshoot in the curve is not identifiable. Ideally, one would look for a clear signature for the cage breaking in $g(\mathbf{r}, t)$, but we have not found a single criterion applicable over the whole range of Pe and ϕ: At $\phi = 0.4$ and moderate Pe, however, we can say that the cage breaking occurs by detachment of the cage in the extensional quadrant close to the x axis. This can be seen in Fig. 17(b), which shows the deformation of the cage in the shear plane. The solid circle drawn on each image is the estimate of the cage deformation given by $r - 2 = \dot{\gamma}t + \sqrt{\dot{\gamma}t/Pe}$. At $Pe = 10^4$, however, the cage structure (nearest neighbor ring) is found to remain intact to larger distance from contact and to break away from contact. As a consequence, γ^{escape} is estimated by fitting the curve to the γ^{pk} points from our simulation. When Brownian motion contributes to the total deformation of the cage, the overshoot is predicted to occur at

$$\frac{\gamma^{pk}}{\gamma^{\text{escape}}} = \frac{1}{4}\left(\sqrt{\frac{1}{Pe\,\gamma^{\text{escape}}} + 4} - \sqrt{\frac{1}{Pe\,\gamma^{\text{escape}}}}\right)^2. \qquad (24)$$

For $\phi = 0.4, 0.45, 0.50$, and 0.56, we can take an escape strain $\gamma^{\text{escape}} = 0.8$, 0.6, 0.55, and 0.46, respectively, to predict the location of the stress overshoots. Figure 18(a) shows the location of the overshoots at these ϕ values against the predictions from this model. The Pe dependence is captured and the location of the overshoots from ASD simulations are close to those calculated from the model. Figure 18(a) also shows experimental results of Laurati *et al.* [20] and Koumakis *et al.* [19] at $\phi = 0.56$. These show the same basic dependence on $\overline{Pe}$ as our ASD results. In Fig. 18(a), the Pe used for the experimental and ASD results is the rescaled $\overline{Pe}$ from Brady [32], which takes the loss of mobility of the particles with volume fraction into account: $\overline{Pe} = Pe/D_0^s(\phi)$, with $D_0^s(\phi)$ the short time self-diffusivity of the suspension

(made dimensionless with D_0). Figure 18(b) shows the Brownian shear stress during start-up of shear flow at $\phi = 0.4$ for different Pe and the strain at overshoot predicted by Eq. (24). We rescale the shear stress σ^B_{xy} by its steady value and the shear strain by its value at the peak of the overshoot in the Brownian stress. This leads to the collapsed stress curve in Fig. 18(c). For all Pe, steady state is reached for $\gamma/\gamma^{pk} \approx 2$. The magnitude of the overshoot depends on the strength of the flow.

b. Structure. At equilibrium, the pair distribution function $g(\mathbf{r})$ is isotropic. The concentric rings depicted in the first image at each Pe in Figs. 19(b)–19(d) are typical for a hard-sphere liquid. As the shearing starts, particles accumulate in the compressional quadrant as shown in Figs. 19(b)–19(d) in the second pictures. The particles near the extensional axis are convected away, creating a depletion zone. After a strain of $\dot{\gamma}t = 0.6$, for the higher shear rates at $Pe = 5$ and $Pe = 50$, we see that the ring of particles close to contact is distorted, but this ring is not yet broken. This ring can be understood as being the cage of neighbors around the particle. The overshoot in the Brownian stresses takes place as this high probability region is broken up when the particle escapes the cage of neighbors. For $Pe = 0.5$, the overshoot happens at $\dot{\gamma}t \approx 0.4$, and we can observe that the neighbor cage is already broken for $\dot{\gamma}t \approx 0.6$. At the stress overshoot, the value of $g(\mathbf{r},t)$ in the compressional quadrant goes through a maximum for the nearest neighbor and the second neighbor peak. This behavior has also been observed for the nearest neighbor peak by Zausch *et al.* [23] and Amann *et al.* [21]. For $Pe = 0.5$, the microstructure for $\dot{\gamma}t > 1.4$ appears fully developed. For $Pe = 50$, it takes a strain of $\dot{\gamma}t \approx 2$ to achieve a nearly steady appearance of the microstructure. The fourth image in each row of Figs. 19(b)–19(d) shows the microstructure at $\dot{\gamma}t = 5$, immediately prior to cessation of flow. The parallel layers in the velocity gradient direction appearing in the shear plane for $Pe = 5$ and $Pe = 50$ indicate partial ordering. Once the shear flow is stopped, Brownian motion relaxes the structure. In the fifth image of Figs. 19(c) and 19(d), the boundary layer near the compressional axis at $Pe = 5$ and $Pe = 50$ spreads as the particles move away from contact. At this point, for $Dt/a^2 = 0.06$, most of the shear stress has relaxed with the diffusion of the boundary layer (see Fig. 13) while the larger scale reorganization requires a longer time. Confocal microscopy can capture the positions of particles with an accuracy of 20–100 nm [62,63]. As the thickness of the boundary layer around a particle scales as $(Pe^{-1}a)$, a being the radius of the particle, for colloidal particles used in confocal microscopy with a diameter $\approx 1\,\mu$m, as used by Xu and Gilchrist [62] and Lin *et al.* [63], this

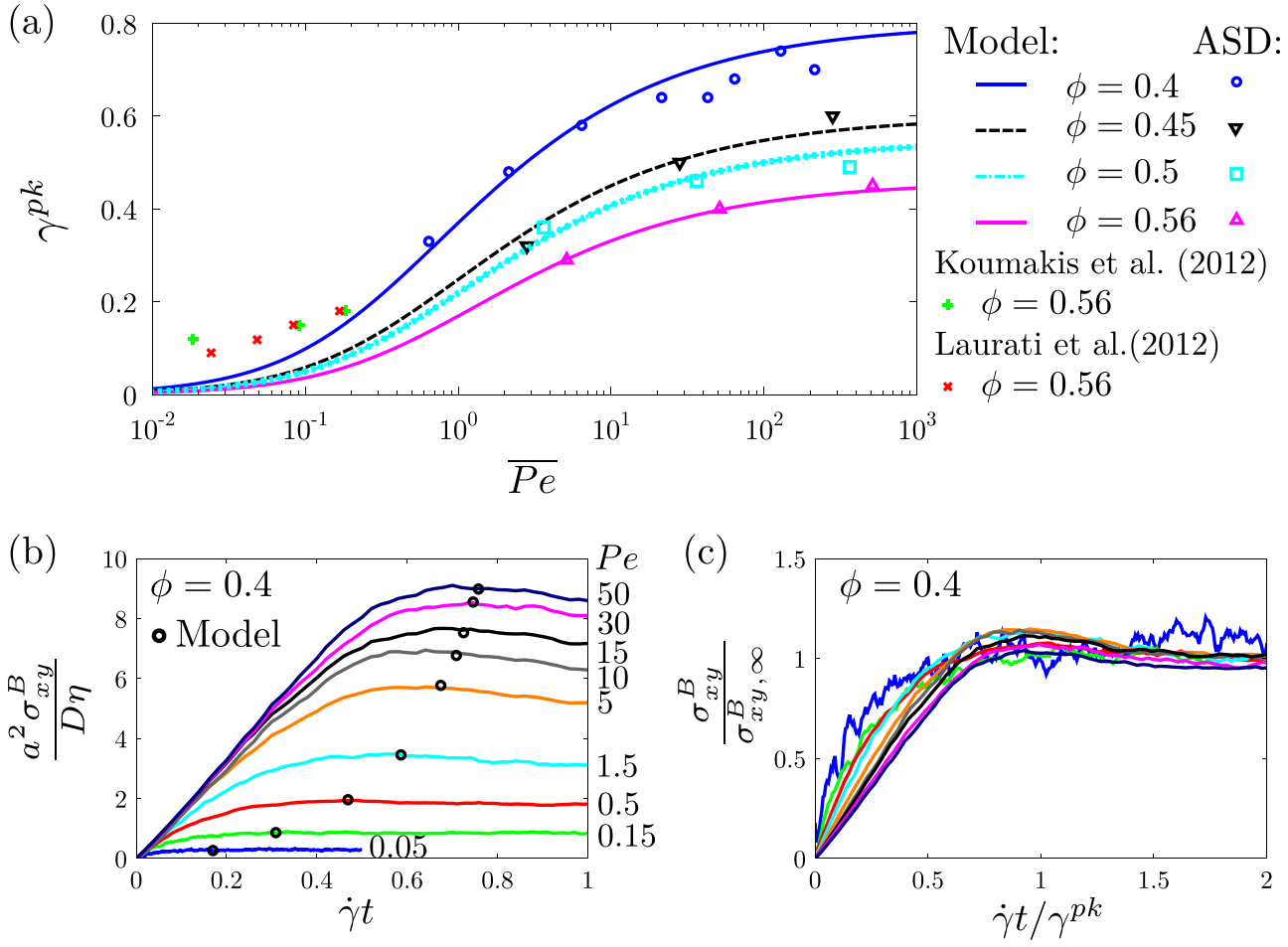

FIG. 18. The Brownian shear stress during start-up of shear flow at different Pe and ϕ. (a) Model predictions for different γ^{escape} are shown along with ASD results at $\phi = 0.4$–0.56 and experimental results of Koumakis *et al.* [19] and Laurati *et al.* [20] at $\phi = 0.56$. In (b), the open circles show where the model predicts the overshoot to be. (c) The shear stress rescaled by its steady state value plotted as a function of the deformation scaled by its value at the peak stress.

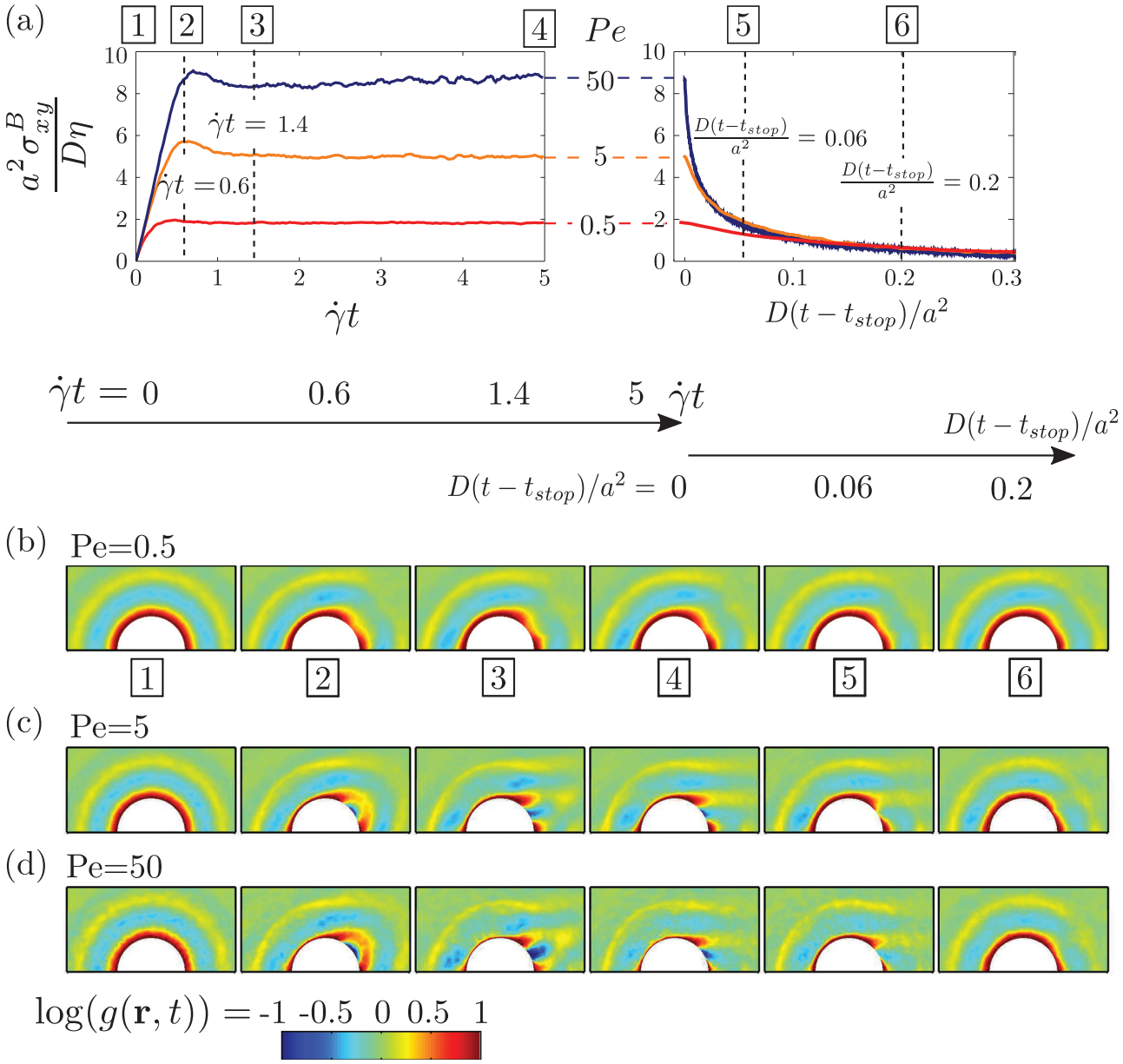

FIG. 19. The (a) shear stress and snapshots of $g(\mathrm{r}, t)$ during the start-up and cessation of the shear flow for (b) $Pe = 0.5$, (c) $Pe = 5$, and (d) $Pe = 50$ at a volume fraction $\phi = 0.4$ simulated by ASD with $N = 512$. The suspension starts at equilibrium and undergoes the start-up of the shear flow. The flow is stopped after $\gamma = 5$. After flow is stopped, the snapshots of $g(\mathbf{r}, t)$ are taken after the same diffusive times. Video 1: Start-up and cessation of shear flow for $Pe = 0.5$, $\phi = 0.4$ [URL: http://dx.doi.org/10.1122/1.4979005.1]; Video 2: Start-up and cessation of shear flow for $Pe = 5$, $\phi = 0.4$ [URL: http://dx.doi.org/10.1122/1.4979005.2]; Video 3: Start-up and cessation of shear flow for $Pe = 50$, $\phi = 0.4$ [URL: http://dx.doi.org/10.1122/1.4979005.3]

suggests that the length scale involved in the boundary layer relaxation can be captured accurately up to $Pe \approx 10$. At larger Pe, where the boundary layer thickness is $\delta < 50$ nm, the stress-optical rule used to calculate stresses from confocal microscopy images would not capture the rapid initial decay of the shear stress after cessation of shear flow.

We can also compare the decay of N_1^B and N_2^B after cessation of shear flow with the relaxation of the microstructure: Comparing Figs. 14 and 15, we see that N_2^B has a fast relaxation which is simultaneous with the relaxation of the boundary layer while N_1^B, like the larger-scale reorganization of the microstructure including wake closure, takes longer to approach equilibrium. In the last image of each row in Figs. 19(b)–19(d), the equilibrium microstructure has been almost completely recovered. The evolution of the microstructure during the start-up and cessation of shear flow can also be seen in the videos for $Pe = 0.5$, $Pe = 5$, and $Pe = 50$ [Fig. 19 (Multimedia view)].

VI. CONCLUSIONS

We have probed the dynamics of a hard-sphere colloidal dispersion in transient shear flow. Complex fluid behavior, or non-Newtonian rheology, is a result of the coupling of the motions of microscopic elements in a material to the bulk motion, and here the microscopic elements are identical spheres. While it is in some sense the simplest of complex fluids, understanding of the hard-sphere dispersion rheology

requires consideration of the correlated dynamics and resulting microstructural arrangement of particles, reflected in the present work by the pair distribution function $g(\mathbf{r})$. The transient dynamics in start-up flow and diffusive relaxation of a steady shear-induced microstructure provide insight to the relevant length and time scales involved in the rearrangements under flow. Here, we have probed these behaviors over a wide range of shear rates stated as the dimensionless Péclet number, $Pe = 3\pi\eta\dot{\gamma}a^3/kT$, and solid volume fraction, ϕ, for monodisperse spheres. We have studied this system by dynamic simulation, by BD without HI for ease of comparison with analytical theory based on the Smoluchowski equation and by ASD to probe a close replica of the realistic dynamics including HI. To elucidate the role of the balance between shear flow and Brownian motion in a concentrated suspension, our focus in presenting the results of the study has been on the Pe-dependence of the microstructure and stress at the solid fraction $\phi = 0.4$, with limited results at other concentrations.

Simulation of the transient dynamics of a dispersion requires a different approach than is usually applied to study of steady shear flow. In steady shear, ergodicity allows time averages of quantities to replace ensemble averages, and good statistical accuracy for properties and structure may be achieved by sampling from one or several extended-time simulations. To achieve similar accuracy in a transient condition, one must use a much larger number of particles. Alternatively, many replicas of the same simulation conditions with a similar number of particles will suffice, and we use this approach. In the results presented for the transient dynamics in the case of ASD, we have typically simulated $O(1000)$ replicas (each simulating the dynamics of $N = 512$ particles in the computational unit cell), starting in all cases from initial conditions drawn from an equilibrium ensemble and then subjected to flow at the desired condition. Flow cessation was studied after reaching steady state in these same simulations, and thus has the same statistical sampling.

The ability to conveniently study a large number of replicas arises from the recent availability of large numbers of equivalent fast processors and large dynamic memory in computational clusters. We have taken advantage of this advance in computational resources to reconsider the steady shear flow behavior of concentrated suspensions, in particular using larger numbers of particles in the unit cell than had been applied in prior work [9–11,49]. This has, for the most part, confirmed the general findings of prior work, but for normal stress differences at near-equilibrium conditions, we now are able to see the expected approach to zero of both N_1 and N_2 which was not found in the work of Foss and Brady [10]; we show that $N = 27$ as applied in Foss and Brady showed larger average response, as well as a quasiperiodic behavior, in the normal stress differences at small Pe, with both $N_1/\eta\dot{\gamma}$ and $N_2/\eta\dot{\gamma}$ growing in magnitude as $Pe \to 0$. For $N = 512$, the expected trend toward zero of these normalized stress differences was realized. The stronger response and quasiperiodic behavior at near-equilibrium conditions, $Pe \ll 1$, for small N appears to be due to reduced configurational freedom, or greater packing constraints, at smaller N. One may conjecture that this is a result of N-dependence of the maximum random close packing fraction, $\phi_{\max}$; while we have not explored this point, this suggests that size dependence of properties at larger ϕ may persist to larger N.

Turning now to the transient behavior, the near-equilibrium dynamics of the hard-sphere dispersion was explored through the quiescent shear stress autocorrelation function from simulations. The linear response deduced from this analysis was shown to exhibit a divergent value of the high-frequency elastic modulus, G'_∞, in the absence of HI (computations by BD), with this divergence eliminated by inclusion of HI (computations by ASD). These findings are consistent with a near-equilibrium analysis of the Smoluchowski equation for pair correlation at high frequency described in Sec. III B, in which the development of a boundary layer associated with the no-flux condition at pair contact yields an infinite G'_∞ for suspensions without HI but a finite G'_∞ for suspensions with HI. The elastic modulus values from ASD simulations at $Pe = 0$ agree reasonably well with experimental data [58].

The well-known boundary-layer and wake structure [11] of the pair distribution function, $g(\mathbf{r})$, described for steady dilute conditions in the work of Brady and Morris [8], captures the structural anisotropy needed to rationalize qualitative aspects of the normal stress differences in the dispersion. The development of the boundary layer structure from, and its relaxation back toward, the equilibrium isotropic condition has been analyzed here, showing a buildup toward the steady state near the compressional axis at short times scaling as $t^{1/2}$ (with viscosity growth scaling in the same way), with later growth on the flow timescale ($\dot{\gamma}^{-1}$). While the structure is predicted to approach the asymptotic steady value exponentially, simulation shows stress overshoots reflective of structural features not predicted by dilute theory. The boundary layer of pair correlation is predicted to be $\delta \sim Pe^{-1}a$ in thickness, and the diffusive relaxation of the microstructure is thus initially with the rapid time scale $\delta^2/D = Pe^{-2}a^2/D$. For $Pe \gg 1$, the initial relaxation is thus very rapid, occurring on times much shorter than predicted by the time scale for diffusion on the particle scale, a^2/D.

Our focus in analysis of the transients from the simulations has been on the stress response and determination of the key structural features leading to the observed behavior. The stress is split into its Brownian and hydrodynamic components in the ASD simulations and the Brownian shear stress during start-up is shown to initially be consistent with $\sigma^B_{xy} \sim G'\gamma = G'\dot{\gamma}t$, with G' the elastic modulus determined from a Green-Kubo analysis. Deviation from this behavior occurs earlier for smaller Pe and for $\phi \leq 0.4$ is found to drop below the elastic stress prediction, while for $\phi > 0.4$, $\sigma^B_{xy} > G'\dot{\gamma}t$ is observed for large Pe: This behavior is suggestive of the strongly nonlinear elastic stress generated by the neighbor "cage" and we return to this concept below. At the $\phi = 0.4$ conditions on which we have focused, the Brownian stresses overshoot the magnitude of their steady state values for all of the viscometric functions for $Pe > 1$, while the hydrodynamic stress components asymptotically approach their steady magnitudes; for comparison to experiment, it is useful to note that the total stress overshoots its steady magnitude due to the Brownian contribution.

The stress overshoots noted above are reflective of Brownian motion generating a flux toward equilibrium as flow-induced distortion of the structure accumulates. This is captured through the neighbor cage concept familiar in the study of colloidal glasses. We find that the concept of the cage is meaningful down to much lower ϕ than the glass transition value, in suspensions which show no yield stress. In particular, we find that the maximum Brownian shear stress in start-up flow (i.e., the viscosity at peak overshoot) is associated with the escape of the particle from its neighbor cage. This event can be observed structurally through the evolution of the nearest neighbor ring. The rupture dynamics of this ring are, however, not identical at all conditions, so that we were not able to establish a unique structural signature for the cage rupture.

The dilute Smoluchowski analysis prediction for flow cessation, with rapid boundary layer decay, is observed, but is accompanied by a slower decay at larger length scales, largely due to the need to move distances of $O(a)$ to relax structural distortion in the nearest neighbor ring (wake closure) and beyond. The two time scales of relaxation of structure are reflected in different relaxation dynamics of the various viscometric functions. Noting that upon flow cessation it is only the Brownian stresses which remain and undergo relaxation, their initial slope of relaxation depends on the precessation shear flow (the stronger the flow, the steeper the initial slope). This initial decay is much faster for σ_{xy}^B and N_2^B than N_1^B, reflecting the strong dependence of the first two functions on the boundary layer structure. After this initial relaxation, both σ_{xy}^B and N_1^B collapse and have a slow algebraic relaxation. For N_2^B at high Pe, the fast relaxation after cessation leads to a change in sign, and the resulting small positive value then has a slow relaxation. The results of the present work illustrate that the stresses in start-up flow can be related to the equilibrium system behavior for early transient and the departure from equilibrium may be related to the dynamics of a well-defined cage formed by the nearest neighbors. The relaxation dynamics in flow cessation requires consideration of the fast relaxation dynamics in the boundary layer combined with the slower large-scale reorganization of the microstructure. These concepts may be useful to the development of microstructurally based constitutive modeling of colloidal dispersion rheology.

ACKNOWLEDGMENTS

This work was supported by NSF PREM (Award No. DMR-0934206) and by NSF CBET (Award No. 1605283). This research was also supported, in part, by a grant of computer time from the City University of New York High Performance Computing Center under NSF Grant Nos. CNS-0855217, CNS-0958379, and ACI-1126113.

APPENDIX A: STEADY STATE SOLUTION TO THE SMOLUCHOWSKI EQUATION

We are interested in the behavior far from equilibrium where $Pe \gg 1$ in the absence of HI. The relative velocity is equal to that of the imposed shear flow, $\mathbf{U}^\infty = \dot{\mathbf{\Gamma}} \cdot \mathbf{r}$ and the pair diffusivity is a constant and equal to $2D$; thus the equations system (4) reduces to

$$\frac{\partial g}{\partial t} - \nabla^2 g + Pe\, \dot{\mathbf{\Gamma}} \cdot \mathbf{r} \cdot \nabla g = 0, \tag{A1a}$$

$$\frac{\partial g}{\partial r} = 2Pe\gamma_r g \quad \text{at } r = 2, \tag{A1b}$$

$$g \sim 1 \quad \text{as } r \to \infty, \tag{A1c}$$

where we use the notation $\gamma_r = \hat{\mathbf{r}} \cdot \hat{\mathbf{E}} \cdot \hat{\mathbf{r}}$.

As shown by Brady and Morris [8], at large Pe in steady state, Eq. (A1a) reduces to $\dot{\mathbf{\Gamma}} \cdot \mathbf{r} \cdot \nabla g = 0$, i.e., on a streamline g is a constant, which Eq. (A1c) shows to be unity. This constant solution does not satisfy the no-flux boundary condition at contact, however, and there is a boundary layer in which the effects of Brownian motion balance those of advection. The relevant length scale is no longer the particle radius but the thickness of the boundary layer, $\delta \sim aPe^{-1}$. Also, the appropriate diffusive time scale is that needed for a particle to diffuse across the boundary layer, $\delta^2/2D$, rather than $a^2/2D$. Thus, we stretch r and t according to

$$y = Pe(r-2) \quad \text{and} \quad \tau = tPe^2. \tag{A2}$$

The governing equation and boundary conditions for g in the stretched coordinates are

$$\frac{\partial g}{\partial \tau} - \frac{\partial^2 g}{\partial y^2} + 2\gamma_r \left[1 - Pe^{-1}\frac{1}{2\gamma_r}(1-\gamma_r y)\right]\frac{\partial g}{\partial y} = -Pe^{-1}\left[\gamma_\theta \frac{\partial g}{\partial \theta}\right] + O(Pe^{-2}), \tag{A3a}$$

$$\frac{\partial g}{\partial y} = 2\gamma_r g \quad \text{at } y = 0, \tag{A3b}$$

$$g \sim 1 \quad \text{as } y \to \infty, \tag{A3c}$$

where θ is the azimuthal angle measured from the z-axis, and ϕ is the polar angle measured from the x-axis. In Eqs. (A3a)–(A3c), γ_r, γ_θ, and γ_ϕ are defined by

$$\gamma_r = \hat{\mathbf{r}} \cdot \hat{\mathbf{\Gamma}} \cdot \hat{\mathbf{r}} = \hat{\mathbf{r}} \cdot \hat{\mathbf{E}} \cdot \hat{\mathbf{r}}, \quad \gamma_\theta = \hat{\theta} \cdot \hat{\mathbf{\Gamma}} \cdot \hat{\mathbf{r}}, \quad \gamma_\phi = \hat{\phi} \cdot \hat{\mathbf{\Gamma}} \cdot \hat{\mathbf{r}},$$

where $\hat{\theta}$ and $\hat{\phi}$ are the unit vectors in the θ- and ϕ-directions, respectively, and $\hat{\mathbf{\Gamma}}$ is the nondimensional velocity-gradient tensor.

Brady and Morris [8] show that the terms of $O(Pe^{-1})$ must be retained in the equation for g, and simplify the problem by keeping only those terms on the left-hand side of Eq. (A3a) in a "radial-balance approximation" (meaning angular derivatives are neglected) as the competition between radial advection and diffusion is what generates the large gradients in g characteristic of the boundary layer. The steady-state solution to the radial-balance approximation is

$$g_{ss}(y) = \frac{1 + 2\gamma_r \int_0^y e^{s(z)} dz}{1 + 2\gamma_r \int_0^\infty e^{s(z)} dz},$$

where $s(z)$ is given by

$$s(z) = 2\gamma_r\left[\left(1 - \frac{1}{2\gamma_r}Pe^{-1}\right)z + \frac{1}{4}Pe^{-1}z^2\right].$$

APPENDIX B: SOLUTION TO THE SMOLUCHOWSKI EQUATION FOR START-UP OF SHEAR FLOW

For start-up flow, the initial condition is the isotropic equilibrium structure, $g = 1$, and it is again useful to analyze the problem in terms of the deviation from this structure denoted by $f = g - 1$. On taking the Laplace transform, which we denote by $\tilde{}$, and with s conjugate to τ, Eqs. (A3a)–(A3c) in the radial-balance approximation become

$$\frac{\partial^2\tilde{f}}{\partial y^2} - 2\gamma_r\left[1 - Pe^{-1}\frac{1}{2\gamma_r}(1 - \gamma_r y)\right]\frac{\partial\tilde{f}}{\partial y} - s\tilde{f} = 0, \tag{B1a}$$

$$\frac{\partial\tilde{f}}{\partial y} - 2\gamma_r\tilde{f} = \frac{2\gamma_r}{s} \quad \text{at } y = 0, \tag{B1b}$$

$$\tilde{f} \sim 0 \quad \text{as } y \to \infty. \tag{B1c}$$

The factor of $1/s$ in Eq. (B1b) is a result of the Heaviside step function in time necessary because $\gamma_r = 0$ before the inception of the flow. A change of variables transforms (B1) to

$$\frac{\partial^2\tilde{f}}{\partial x^2} + 2x\frac{\partial\tilde{f}}{\partial x} - \sigma\tilde{f} = 0, \tag{B2a}$$

$$\frac{\partial\tilde{f}}{\partial x} + 2\beta\tilde{f} = \frac{-8Pe^2}{\beta\sigma} \quad \text{at } x = x_0 = \frac{\beta^2 + 1}{\beta}, \tag{B2b}$$

$$\tilde{f} \sim 0 \text{ as } x \to \infty. \tag{B2c}$$

where

$$\beta = (-2\gamma_r Pe)^{1/2},$$
$$x = \beta\left(1 - \frac{1}{2\gamma_r}Pe^{-1} + \frac{1}{2}Pe^{-1}y\right),$$

and

$$\sigma = \frac{4Pe^2}{\beta^2}s.$$

This problem has two linearly independent solutions in terms of the confluent hypergeometric function [64]

$$xe^{-x^2}M\left(1 + \frac{\sigma}{4}, \frac{3}{2}, x^2\right) \quad \text{and} \quad xe^{-x^2}U\left(1 + \frac{\sigma}{4}, \frac{3}{2}, x^2\right). \tag{B3}$$

For calculation of the rheological properties [cf. Eq. (15)] only the value at contact, $y = 0$ or $x = x_0$, is necessary and this simplifies the analysis. Once the boundary conditions are applied, the contact value of g is

$$g(0,\tau) = 1 + \mathcal{L}^{-1}\left[\tilde{f}(0,s)\right], \tag{B4a}$$

$$\tilde{f}(0,s) = \frac{\beta^2(\beta^2+1)}{1 + \frac{1}{2}\beta^2 - (\beta^2+1)^2\left.\frac{U'}{U}\right|_{x_0}}\frac{1}{s} \tag{B4b}$$

In Eq. (B4a), $\mathcal{L}^{-1}$ represents an inverse Laplace transform and the arguments of U are the same as in Eq. (B3) and are evaluated at $x = x_0$ with the prime representing differentiation with respect to the third argument. We have not been able to carry out the inverse analytically for all times, but the short- and long-time asymptotic behavior can be extracted.

APPENDIX C: SOLUTION TO THE SMOLUCHOWSKI EQUATION FOR CESSATION OF SHEAR FLOW

For the relaxation of the microstructure after cessation of shear flow, we analyze the deviation $f = g - 1$ which, to leading order in Pe, is governed by

$$\frac{\partial^2 f}{\partial y^2} - \frac{\partial f}{\partial\tau} = O(Pe^{-1}), \tag{C1a}$$

$$\frac{\partial f}{\partial y} = 0 \quad \text{at } t = 0, \tag{C1b}$$

$$f \sim 0 \quad \text{as } y \to \infty, \tag{C1c}$$

$$f_0(y,0) = g_{ss}(y) - 1 = 2\gamma_r g_{ss}(o)\int_\infty^y e^{s(z)}dz. \tag{C1d}$$

On taking Laplace transforms, the problem becomes

$$\frac{\partial^2\tilde{f}}{\partial y^2} - s\tilde{f} = -f_0(y), \tag{C2a}$$

$$\frac{\partial\tilde{f}}{\partial y} = 0 \quad \text{at } t = 0, \tag{C2b}$$

$$\tilde{f} \sim 0 \quad \text{as } y \to \infty. \tag{C2c}$$

The resulting system is the same as was found for the microrheology of colloidal suspensions by Zia and Brady [65], the difference here being the value of $f_0(y)$. The solution of this problem is straightforward using variation of parameters. Owing to the δ-function nature of the hard-sphere interparticle force, we need only find the contact value

$$\tilde{f}(0,s) = -g_{ss}(0)\frac{1}{\sqrt{s}(\sqrt{s} - 2\gamma_r)}, \tag{C3}$$

to obtain the rheological behavior. The inverse Laplace transform of Eq. (C3) can be found for all times (see chapter 29 of [64]) and is given by

$$f(0,\tau) = -g_{ss}(0)e^{4\gamma_r^2\tau}\text{erfc}\left(\sqrt{4\gamma_r^2\tau}\right). \tag{C4}$$

References

[1] Batchelor, G. K., "The effect of Brownian motion on the bulk stress in a suspension of spherical particles," J. Fluid. Mech. **83**, 97–117 (1977).

[2] Tough, R. J. A., P. N. Pusey, H. N. W. Lekkerkerker, and C. Van Den Broeck, "Stochastic descriptions of the dynamics of interacting Brownian particles," Mol. Phys. **59**, 595–619 (1986).

[3] Dhont, J. K. G., *An Introduction to Dynamics of Colloids* (Elsevier, Amsterdam, 1996).

[4] Russel, W. B., and A. P. Gast, "Nonequilibrium statistical mechanics of concentrated colloidal dispersions: Hard spheres in weak flows," J. Chem. Phys. **84**, 1815–1826 (1986).

[5] Wagner, N. J., and B. J. Ackerson, "Analysis of nonequilibrium structures of shearing colloidal suspensions," J. Chem. Phys. **97**, 1473–1483 (1992).

[6] Brady, J. F., and M. Vicic, "Normal stresses in colloidal dispersions," J. Rheol. **39**, 545–566 (1995).

[7] Lionberger, R. A., "Shear thinning of colloidal dispersions," J. Rheol. **42**, 843–863 (1998).

[8] Brady, J. F., and J. F. Morris, "Microstructure of strongly sheared suspensions and its impact on rheology and diffusion," J. Fluid. Mech. **348**, 103–139 (1997).

[9] Phung, T. N., J. F. Brady, and G. Bossis, "Stokesian dynamics simulations of Brownian suspensions," J. Fluid. Mech. **313**, 181–207 (1996).

[10] Foss, D. R., and J. F. Brady, "Structure, diffusion and rheology of Brownian suspensions by Stokesian dynamics simulation," J. Fluid. Mech. **407**, 167–200 (2000).

[11] Morris, J. F., and B. Katyal, "Microstructure from simulated Brownian suspension flows at large shear rate," Phys. Fluids **14**, 1920–1937 (2002).

[12] Nazockdast, E., and J. F. Morris, "Pair-particle dynamics and microstructure in sheared colloidal suspensions: Simulation and Smoluchowski theory," Phys. Fluids **25**, 070601 (2013).

[13] Nazockdast, E., and J. F. Morris, "Microstructural theory and the rheology of concentrated colloidal suspensions," J. Fluid. Mech. **713**, 420–452 (2012).

[14] Hyun, K., M. Wilhelm, C. Klein, K. S. Cho, J. G. Nam, K. H. Ahn, S. J. Lee, R. H. Ewoldt, and G. H. McKinley, "A review of nonlinear oscillatory shear tests: Analysis and application of large amplitude oscillatory shear (LAOS)," Prog. Polym. Sci. **36**, 1697–1753 (2011).

[15] Banchio, A. J., and J. F. Brady, "Accelerated Stokesian dynamics: Brownian motion," J. Chem. Phys. **118**, 10323–10332 (2003).

[16] D'Haene, P., J. Mewis, and G. G. Fuller, "Scattering dichroism measurements of flow-induced structure of a shear thickening suspension," J. Colloid Interface Sci. **156**, 350–358 (1993).

[17] van der Werff, J. C., C. G. de Kruif, C. Blom, and J. Mellema, "Linear viscoelastic behavior of dense hard-sphere suspensions," Phys. Rev. A **39**, 795–807 (1989).

[18] Yziquel, F., P. J. Carreau, M. Moan, and P. A. Tanguy, "Rheological modeling of concentrated colloidal suspensions," J. Non-Newtonian Fluid. Mech. **86**, 133–155 (1999).

[19] Koumakis, N., M. Laurati, S. U. Egelhaaf, J. F. Brady, and G. Petekidis, "Yielding of hard-sphere glasses during start-up shear," Phys. Rev. Lett. **108**, 098303 (2012).

[20] Laurati, M., K. J. Mutch, N. Koumakis, J. Zausch, C. P. Amann, A. B. Schofield, G. Petekidis, J. F. Brady, J. Horbach, M. Fuchs, and S. U. Egelhaaf, "Transient dynamics in dense colloidal suspensions under shear: Shear rate dependence," J. Phys.: Condens. Matter **24**, 464104 (2012).

[21] Amann, C. P., D. Denisov, M. T. Dang, B. Struth, P. Schall, and M. Fuchs, "Shear-induced breaking of cages in colloidal glasses: Scattering experiments and mode coupling theory," J. Chem. Phys. **143**, 034505 (2015).

[22] Koumakis, N., M. Laurati, A. R. Jacob, K. J. Mutch, A. Abdellali, A. B. Schofield, S. U. Egelhaaf, J. F. Brady, and G. Petekidis, "Start-up shear of concentrated colloidal hard spheres: Stresses, dynamics, and structure," J. Rheol. **60**, 603–623 (2016).

[23] Zausch, J., J. Horbach, M. Laurati, S. U. Egelhaaf, J. M. Brader, T. Voigtmann, and M. Fuchs, "From equilibrium to steady state: The transient dynamics of colloidal liquids under shear," J. Phys.: Condens. Matter **20**, 404210 (2008).

[24] Sierou, A., and J. F. Brady, "Rheology and microstructure in concentrated noncolloidal suspensions," J. Rheol. **46**, 1031–1056 (2002).

[25] Kulkarni, S. D., and J. F. Morris, "Ordering transition and structural evolution under shear in Brownian suspensions," J. Rheol. **53**, 417–439 (2009).

[26] Mackay, M., and B. Kaffashi, "Stress jumps of charged colloidal suspensions, measurement of the elastic-like and viscous-like stress components," J. Colloid Interface Sci. **174**, 117–123 (1995).

[27] O'Brien, V. T., and M. Mackay, "Stress components and shear thickening of concentrated hard sphere suspensions," Langmuir **16**, 7931–7938 (2000).

[28] Ballauff, M., J. M. Brader, S. U. Egelhaaf, M. Fuchs, J. Horbach, N. Koumakis, M. Laurati, K. J. Mutch, G. Petekidis, M. Siebenbuerger, Th. Voigtmann, and J. Zausch, "Residual stresses in glasses," Phys. Rev. Lett. **110**, 215701 (2013).

[29] Fuchs, M., and M. E. Cates, "Theory of nonlinear rheology and yielding of dense colloidal suspensions," Phys. Rev. Lett. **89**, 248304 (2002).

[30] Brader, J. M., M. Siebenbuerger, and M. Ballauff, "Nonlinear response of dense colloidal suspensions under oscillatory shear: Mode-coupling theory and FT-rheology experiments," Phys. Rev. E **82**, 061401 (2010).

[31] Batchelor, G. K., and J. T. Green, "The hydrodynamic interaction of two small freely-moving spheres in a linear flow field," J. Fluid. Mech. **56**, 375–400 (1972).

[32] Brady, J. F., "The rheological behavior of concentrated colloidal suspensions," J. Chem. Phys. **99**, 567–581 (1993).

[33] Yurkovetsky, Y., and J. F. Morris, "Particle pressure in sheared Brownian suspensions," J. Rheol. **52**, 141–164 (2008).

[34] Morris, J. F., "A review of microstructure in concentrated suspensions and its implications for rheology and bulk flow," Rheol. Acta **48**, 909–923 (2009).

[35] Zarraga, I. E., D. A. Hill, and D. T. Leighton, "The characterization of the total stress of concentrated suspensions of noncolloidal spheres in Newtonian fluids," J. Rheol. **44**, 185–220 (2000).

[36] Dai, S., E. Bertevas, F. Qi, and R. Tanner, "Viscometric functions for noncolloidal sphere suspensions with Newtonian matrices," J. Rheol. **57**, 493–510 (2013).

[37] Dbouk, T., L. Lobry, and E. Lemaire, "Normal stresses in concentrated non-Brownian suspensions," J. Fluid. Mech. **715**, 239–272 (2013).

[38] Lootens, D., H. Van Damme, Y. Hemar, and P. Hebraud, "Dilatant flow of concentrated suspensions of rough particles," Phys. Rev. Lett. **95**, 268302 (2005).

[39] Mari, R., R. Seto, J. F. Morris, and M. M. Denn, "Discontinuous shear thickening in Brownian suspensions by dynamic simulation," Proc. Natl. Acad. Sci. U.S.A. **112**, 15326–15330 (2015).

[40] Cwalina, C. D., and N. J. Wagner, "Material properties of the shear-thickened state in concentrated near hard-sphere colloidal dispersions," J. Rheol. **58**, 949–967 (2014).

[41] Royer, J. R., D. L. Blair, and S. D. Hudson, "Rheological signature of frictional interactions in shear thickening suspensions," Phys. Rev. Lett. **116**, 188301 (2016).

[42] Boon, J. P., and S. Yip, *Molecular Hydrodynamics* (Dover Publications, New York, 1980).

[43] Hansen, J.-P., and I. R. McDonald, *Theory of Simple Liquids* (Academic, London, 1986).
[44] Nägele, G., and J. Bergenholtz, "Linear viscoelasticity of colloidal mixtures," J. Chem. Phys. **108**(23), 9893–9904 (1998).
[45] Cichocki, B., and B. U. Felderhof, "Linear viscoelasticity of semi-dilute hard-sphere suspensions," Phys. Rev. A **43**, 5405–5411 (1991).
[46] Lionberger, R. A., and W. B. Russel, "High frequency modulus of hard sphere colloids," J. Rheol. **38**(6), 1885–1908 (1994).
[47] Verberg, R., I. M. de Schepper, M. J. Feigenbaum, and E. G. D. Cohen, "Square root singularity in the viscosity of neutral colloidal suspensions at large frequencies," J. Stat. Phys. **87**, 1037–1049 (1997).
[48] Allen, M. P., and D. J. Tildesley, *Computer Simulation of Liquids* (Clarendon, New York, 1989).
[49] Brady, J. F., and G. Bossis, "Stokesian dynamics," Ann. Rev. Fluid. Mech. **20**, 111–157 (1988).
[50] Heyes, D. M., and J. R. Melrose, "Brownian dynamics simulation of model hard-sphere suspensions," J. Non-Newtonian Fluid. Mech. **46**, 1–28 (1993).
[51] Foss, D. R., and J. F. Brady, "Brownian dynamics simulation of hard-sphere colloidal dispersions," J. Rheol. **44**, 629–651 (2000).
[52] Foss, D. R., and J. F. Brady, "Self-diffusion in sheared suspensions by dynamic simulation," J. Fluid. Mech. **401**, 243–274 (1999).
[53] Lees, A. W., and S. F. Edwards, "The computer study of transport processes under extreme conditions," Solid State Phys. **5**, 1921–1930 (1972).
[54] Rintoul, M. D., and S. Torquato, "Computer simulations of dense hard-sphere systems," J. Chem. Phys. **105**, 9258–9265 (1996).
[55] Clarke, A. S., and J. D. Wiley, "Numerical simulation of the dense random packing of a binary mixture of hard spheres: Amorphous metals," Phys. Rev. B **35**(14), 7350–7356 (1987).
[56] Sierou, A., and J. F. Brady, "Accelerated Stokesian dynamics simulations," J. Fluid. Mech. **448**, 115–146 (2001).
[57] Swan, J., E. Furst, and N. J. Wagner, "The medium amplitude oscillatory shear of semi-dilute colloidal dispersions. Part I: Linear response and normal stress differences," J. Rheol. **58**, 307–337 (2014).
[58] Shikata, T., and D. S. Pearson, "Viscoelastic behavior of concentrated spherical suspensions," J. Rheol. **38**, 601–616 (1994).
[59] Pusey, P. N., and W. van Megen, "Observation of a glass transition in suspensions of spherical colloidal particles," Phys. Rev. Lett. **59**, 2083–2086 (1987).
[60] van Megen, W., and S. M. Underwood, "Glass transition in colloidal hard spheres: Measurement and mode-coupling theory analysis of the coherent intermediate scattering function," Phys. Rev. E **49**, 4206–4220 (1994).
[61] Weeks, E. R., and D. A. Weitz, "Properties of cage rearrangements observed near the colloidal glass transition," Phys. Rev. Lett. **89**, 095704 (2002).
[62] Xu, B., and J. Gilchrist, "Microstructure of sheared monosized colloidal suspensions resulting from hydrodynamic and electrostatic interactions," J. Chem. Phys. **140**(20), 204903 (2014).
[63] Lin, N. Y. C., J. H. McCoy, X. Cheng, B. Leahy, J. N. Israelachvili, and I. Cohen, "A multi-axis confocal rheoscope for studying shear flow of structured fluids," Rev. Sci. Instrum. **85**(3), 033905 (2014).
[64] Abramowitz, M., and I. A. Stegun, *Handbook of Mathematical Functions* (Dover Publications, New York, 1972).
[65] Zia, R. N., and J. F. Brady, "Stress development, relaxation and memory in colloidal dispersions: Transient nonlinear microrheology," J. Rheol. **57**, 457–492 (2013).